Kinetic mechanism and sub-ns measurements of the thermal spark in air

Nicolas Q Minesi, Pierre B Mariotto, Erwan Pannier, Axel Vincent-Randonnier, Gabi Daniel Stancu, Christophe O Laux

Kinetic mechanism and sub-ns measurements of the thermal spark in air

Nicolas Q. Minesi[1,2], Pierre B. Mariotto[1], Erwan Pannier[1], Axel Vincent-Randonnier[3], Gabi Daniel Stancu[1], and Christophe O. Laux[1]

[1] EM2C, CNRS, CentraleSupélec, Université Paris Saclay, 3 Rue Joliot-Curie, 91190 Gif-sur-Yvette, France

[2] Department of Mechanical and Aerospace Engineering, University of California, Los Angeles (UCLA), CA 90095, USA

[3] ONERA – Multi-Physics Department for Energy, Chemin de la Hunière, 91123 Palaiseau, France

E-mail: nicolas.minesi@centralesupelec.fr

Abstract

This experimental and numerical study is focused on the formation of fully ionized plasmas in ambient air by nanosecond pulsed discharges, namely the thermal spark. The first contribution of this article is the experimental characterization of the electron number density during the pulse. An increase of the electron number density up to 10^{19} cm^{-3} was measured with sub-nanosecond resolution via three techniques based on optical emission spectroscopy (OES): Stark broadening of H_α, Stark broadening of N^+/O^+, and the continuum emission of electrons. The discharge diameter is measured with sub-nanosecond resolution using calibrated OES of the N^+ and O^+ lines. All measurements indicate a transition to a micrometric-size filament of fully ionized plasma in approximately 0.5 ns. The second main contribution of this work is the development of a 0-D kinetic mechanism to explain this observation. The mechanism includes 100 reactions, 12 species, and 12 excited electronic states. Particular attention is paid to modeling the N_2, N_2^+, N, and O electronic state kinetics using the electronic states as additional pseudo-species. Our results show that including the electron-impact ionization of the excited electronic states of N and O, in addition to those of N_2, is necessary to explain the experimental results, emphasizing the key role of excited state kinetics in the thermal spark formation.

Keywords: thermal spark, optical emission spectroscopy, ionization cross-section, electronic states, Z-pinch, filamentary discharge, Stark broadening

1. Introduction

In a book that has become a reference in plasma physics, Raizer classified the different types of plasma that can be produced in laboratories and nature. Among the various plasma sources in this ranking, "*the spark discharge stands out sharply*" [1]. In laboratories, a discharge is typically generated between two electrodes when an electric field above the breakdown threshold is applied. If the current is sustained for a time sufficiently long, "*the spark current produces a cathode spot and the spark transforms into [a continuous] arc*" [1]. This transition between the transient spark phase (or "breakdown") and the arc phase was experimentally observed in millisecond discharges employed in the automotive industry for the ignition of combustible mixtures [2]. While the spark phase is typically a non-equilibrium plasma, the arc is at local thermal and chemical equilibrium. For decades, the short duration of nanosecond discharges

has been leveraged to generate non-equilibrium plasmas before their transitions to the arc at thermal equilibrium [3]. These non-equilibrium plasmas can be sustained at a quasi-steady state by repeating the nanosecond discharge at kHz frequencies. Nanosecond repetitively pulsed (NRP) discharges feature rich non-thermal chemistry and therefore present a broad interest in several fields of engineering [4], such as plasma-assisted combustion [5,6] and plasma medicine [7]. They have been studied in various gas mixtures with the electrodes facing open gaps [8–16] or separated by dielectric barriers [17–19].

In air, Pai et al. distinguished three regimes of NRP discharges: (i) NRP-corona, (ii) NRP-glow, and (iii) NRP-spark [9]. A summary of the typical characteristics of these discharges is provided in Table 1. Typical emission spectra of these NRP-corona, glow, and spark discharges in air are dominated by $N_2(B)$ and $N_2(C)$ emissions. The emission of O atoms and $N_2^+(B)$ is also present in the glow and spark regimes. Criteria for the corona-glow and glow-spark transitions were proposed in [9]. The corona and glow discharges are characterized by high voltages, low conduction currents (< 1 A), and low deposited energies (less than 100 µJ per pulse) [9]. These two non-equilibrium discharges produce moderate gas heating (less than 200 K) and relatively low electron number densities (less than 10^{13} cm^{-3} in air at atmospheric pressure) [10]. Corona discharges are confined near the electrodes, whereas the glow and the spark fill the entire interelectrode space. The NRP-spark is characterized by a much higher current (> tens of A) and higher energy deposition (> 1 mJ per mm per pulse) [9,11,20]. The gas temperature in the nanosecond spark was found to increase by thousands of kelvins in a few tens of nanoseconds due to the ultrafast heating mechanism [11,21–24]. Although the electron number density reaches 10^{15}-10^{16} cm^{-3} in the nanosecond non-thermal spark [21], the plasma does not reach equilibrium.

Table 1 Typical parameters of NRP corona, glow [10]**, spark** [11,21]**, and thermal spark** [25,26] [27] **discharges in air near ambient pressure. The deposited electrical energy is estimated for discharge dimensions of approximately 1 mm.**

	Non-equilibrium			Equilibrium
Regime	Corona	Glow	Spark	Thermal spark
Deposited Energy	<10 µJ	~10 µJ	~1 mJ	~1 mJ
Dominant Emission	N_2	N_2	N_2, O	N, O, N^+, O^+
Maximum electron Number Density	$<10^{13}$ cm^{-3}	10^{13} cm^{-3}	10^{15}-10^{16} cm^{-3}	10^{19} cm^{-3}
Temperature Increase	Negligible	<200 K	~1000 K	~40,000 K

However, recent observations of nanosecond discharges do not fit in the three regimes mentioned above. In a study of single microsecond pulses in ambient air, Lo et al. [28] observed a complete ionization of the gas with high electron number densities (10^{18} – 10^{19} cm^{-3}) that do not correspond to any of the discharge regimes described above. The transition from the partially to fully ionized plasma, called "streamer-to-arc" was shorter than 5 ns and accompanied by a dramatic temperature rise, from 1,200 K to 36,000 K, in less than 5 ns. Observations of fully ionized plasmas under nanosecond discharges were also reported in water vapor [29,30] and air [31,32]. Observations of N^+ emission for nanosecond discharges in pin-to-pin configuration were also presented in [33,34]. These authors showed that the "constriction" was accompanied by the emission of "spots" at the electrodes. In a series of papers, Parkevich *et al.* used laser interferometry and low astigmatism lenses to show that the fully ionized discharge propagates in the form of more than ten fully ionized filaments, 10-50 µm in diameter, whereas the discharge looks homogeneous if conventional lenses are used [35–38]. These publications in the 2010s extended the earlier studies performed decades ago for longer discharge durations. In 1977, Stritzke et al. [39] mapped the electron temperature during and after the full ionization using lines of N^+, N^{++}, N^{+++}, and N^{++++}. For the conditions of Stritzke *et al.*, the emission of N^+ appeared at electron number densities above 10^{16} cm^{-3}, and the electron temperature reached 50,000 K. Similar ionization fractions were also measured in 1977 by Albrecht et al. [40] using Stark broadening. In the literature on transient fully ionized plasmas, several denominations were employed by different authors. We recently called this regime "the thermal spark" to distinguish it from the previously observed corona, glow, and non-thermal spark regimes

characterized by Pai et al. [9]. This naming emphasizes the thermal equilibrium state of the plasma (thermal) but also employs the denomination of Raizer for transient discharges (spark) [1].

A counterpart of the thermal spark was concomitantly observed in Surface Dielectric Barrier Discharge (SDBD). Houpt and Leonov [41] showed that the "contraction" of the channel of a 50-µs SDBD in ambient air is associated with the appearance of a continuum spectrum and lines of N^+, N, O, and H_α. Using a 20-ns SDBD, Shcherbanev *et al.* [42] observed a transition from molecular emission to a continuum-dominated spectrum accompanied by an increased Stark broadening of H_α (20-30 nm) and O_{777nm} (5 nm) lines. They named it the "streamer-to-filament" transition [43,44]. The same group measured electron number densities $n_e = 10^{18} – 10^{19}$ cm^{-3} in similar configurations and carefully documented the propagation of the surface fully ionized filaments [42]. More recently, they measured surface filament diameters of 10 µm [45]. These values are comparable to those of Parkevich et al. [35–38,46] observed in pin-to-pin configuration and mentioned earlier. This flagrant similarity in temperature, composition, and spatiotemporal scales suggests that SDBD filaments and thermal sparks share similar kinetics.

It should be noted that the typical timescales of the transition to full ionization are sub-nanosecond, which, added to the micrometric dimensions, make the thermal sparks very challenging to characterize. Nevertheless, our group recently performed sub-nanosecond imaging and optical emission spectroscopy [25] and showed that thermal sparks are generated in five steps: (i) Formation of a partially ionized plasma across the inter-electrodes gap; (ii) Formation of a fully ionized filament at the cathode in less than 0.5 ns. The filament is at thermal equilibrium; (iii) Formation of a similar filament at the anode, delayed compared to the cathode filament; (iv) Propagation of these two fully ionized filaments toward each other; and (v) Merging of the filaments to form the thermal spark. This five-step process matched[1] the observation also reported in [47, p.82]. After the energy deposition ends, the fast electron number density decay was proven to be due to an isentropic expansion during which the plasma remains at equilibrium [25,28,32]. Although the thermal spark formation was experimentally characterized, the reasons behind the abrupt formation of the fully ionized filaments remained unclear, especially the short (0.5 ns) transition from a partially to a fully ionized plasma. To answer these questions, numerical simulations of the thermal spark had to be performed.

Kinetic mechanisms for non-equilibrium discharges already exist in the literature [23,48–52], typically based on the work of Kossyi *et al.* [53] or Capitelli *et al.* [54]. For the streamer-to-filament transition (in SDBD), Shcherbanev et al. [42] performed kinetic simulations (230 Td in N_2 at 6 bar) to explain the fast increase of n_e up to values of about 10^{19} cm^{-3}. The authors reported in their simulation an increase of the ionization degree by three orders of magnitude in 0.25 ns, due mainly to the dissociation and ionization of N_2(B) and N_2(C). However, this mechanism cannot produce ionization fractions above 10%. Therefore, a key mechanism is missing to explain the formation of a fully (100%) ionized plasma in a fraction of a nanosecond. To address this issue, we proposed in Ref. [26] to include the excitation and ionization of the N and O electronic states by electron impact. With this additional set of reactions, the full ionization in air was obtained. However, experimental confirmation of the model's predictions was still needed.

This paper investigates the formation of thermal sparks generated in air by NRP discharges in a pin-to-pin configuration. First, in Section 2, the experimental setup is described. In Section 3, the temporal evolution of the electron number density and the discharge diameter are measured. In Section 4, a kinetic mechanism to explain the phenomenon of full ionization by nanosecond pulses is proposed. Finally, in Section 5, the results of these simulations are validated by comparison with the measurements.

[1] However, some experimental results demonstrated that the filaments formation (step 2. and 3.) were synchronized within 0.5 ns [46,116]. As underlined by [36,46,116], the electrode curvature and surface quality plays a role in the filament formation. The presence of a strong ionic current near the electrode could foster beneficial conditions, such as surface topology or temperature, that could lead to earlier filament formation.

2. Experimental setup

The experimental setup, presented in Figure 1, is extensively described in our previous study [25]. Briefly, a nanosecond discharge is generated (FID FPG 30-100MC4K) at 1 kHz between two pin electrodes separated by 1.2 mm. The experiments are performed in ambient air at 0.1 MPa (humidity below saturation) and within 30 minutes before any erosion of the cathode is noticeable. In specific experiments, we use a mixture of ambient air and H_2 (3.7%) to measure the electron number density from the H_α Stark broadening). The discharge is placed at the focal point of an off-axis parabolic mirror (f = 10 cm), as shown in Figure 1. The collimated light from the plasma is then refocused by a second parabolic mirror (f = 20 cm) onto the monochromator (Acton 500i) entrance slit. The monochromator is equipped with two gratings of 300 and 1800 gr·mm^{-1}, both blazed at 500 nm. An ICCD camera (Pi-MAX4) coupled to the monochromator is used to record the spectra with a gate of 450 ps. The pixel size of the ICCD is 13 µm. A HeNe laser (Thorlabs) is used to determine the instrumental broadening of the optical system. Absolute intensity calibration of the optical system is performed using an integration lamp (OL455, Gooch and Housego).

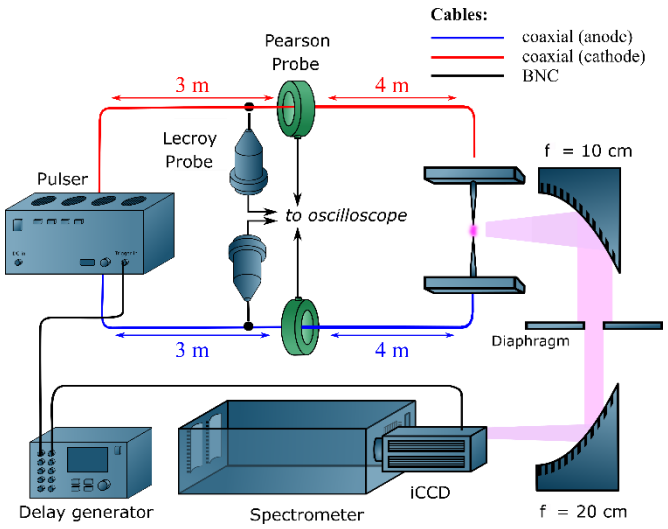

Figure 1 Experimental setup (same as in previous work [25] **except for a change in the length of the coaxial cables).**

The discharge is generated by a positive 10-ns pulse (sent to the anode) and a negative 10-ns pulse (sent to the cathode). Hence, the energy deposition is monitored by two high-voltage probes (LeCroy PPE20kV) and two current transformers (Pearson 6585) connected to an oscilloscope (Lecroy HDO 6104). The measured voltage and current are represented in Figure 2. The voltage and current measurements are performed in the coaxial circuit, 4 meters away from the electrodes. Thus, the incident 10-ns voltage pulse can be separated from the reflected pulse arising due to impedance mismatch.

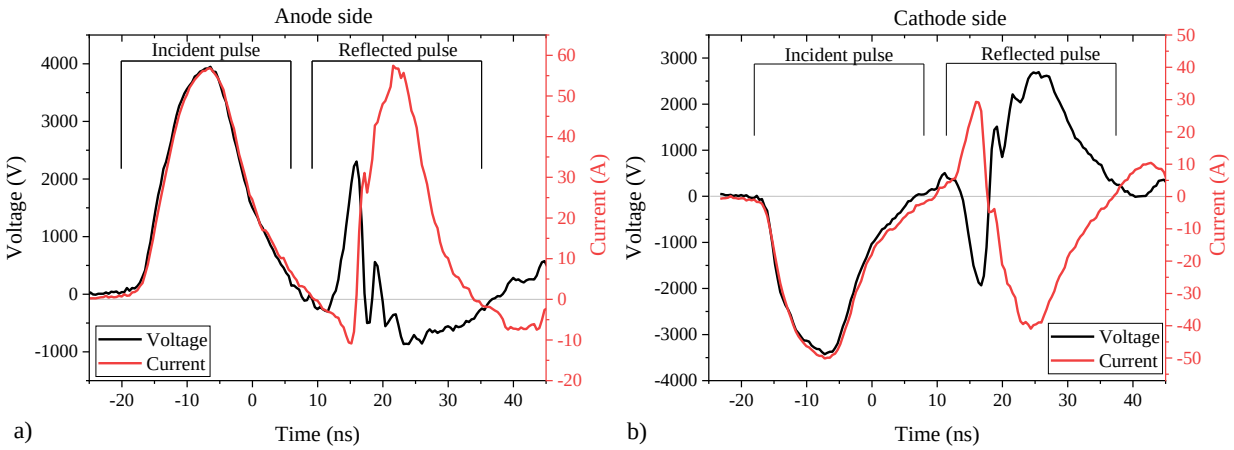

Figure 2 Measured voltage and current on a) the anode and b) the cathode sides. The amplitude difference between the incident pulses at the anode and the cathode is only due to a technical peculiarity of the pulser.

The instantaneous power is the product of the voltage, *U*, and current, *I*. The total energy, *E*, is the time integration of the power in Eq. 1, where the indices 'cat' and 'an' denote the cathode and the anode, respectively.

$$E(t) = E_{cat}(t) + E_{an}(t) = \int_0^t I_{cat}(t)U_{cat}(t)dt + \int_0^t I_{an}(t)U_{an}(t)dt \qquad \text{Eq. 1}$$

In Figure 2, t = 0 ns is defined as the moment the nanosecond pulse reaches the electrode, accounting for the 15-ns delay between the measurement of the voltage rise and its actual arrival at the electrode. As shown in Figure 3, the incident anode and cathode pulses carry 3.9 mJ to the interelectrode gap. Due to an impedance mismatch between the coaxial cable and the plasma, a part of the energy (1.5 mJ) is reflected towards the generator, defined as the upstream direction. Another impedance mismatch on the generator (switched OFF for t > 10 ns) leads to a new reflection. Thus, a 2nd pulse travels in the downstream direction and is detected at t = 75 ns. The second pulse carries ~ 0.8 mJ and deposits ~ 0.25 mJ in the interelectrode gap. For the same reasons, a 3rd pulse is detected at t = 150 ns and deposits another 0.25 mJ. This sequential energy deposition was already observed in previous work [20,25,55] and could explain the "ringing" observed in Ref. [56]. In the comparison of experiments and simulations in Section 5, we restrict the study of the electron number density increase for t < 20 ns, avoiding the complications due to secondary pulses. The instantaneous applied electric field and current, reconstructed from the sum of the incident and reflected pulses at both electrodes, are shown later in Figure 9.

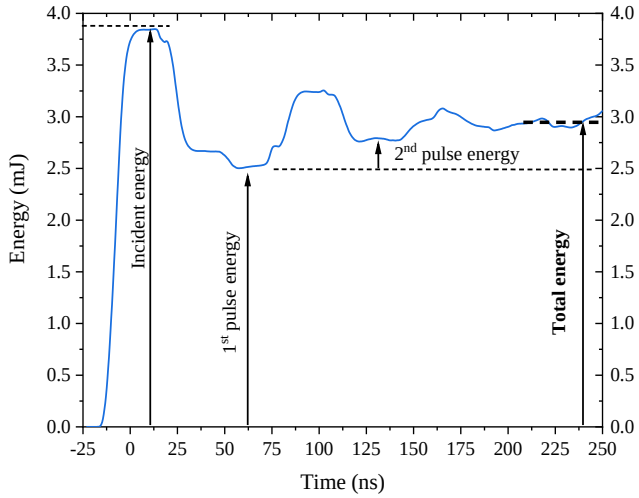

Figure 3 Total transmitted energy according to Eq. 1. Approximately 2.5, 0.25, and 0.25 mJ are deposited in the 1st, 2nd, and 3rd pulses, respectively.

Table 2 Summary of the experimental parameters of this work, compared to those of our previous study [25]**.**

	Previous work		**This work**
	Setup #1 in [25]	Setup #2 in [25]	
Electrode polarities	Cathode-Anode	Cathode-Ground	Cathode-Anode
Interelectrode gap	0.9 mm	2 mm	1.2 mm
Repetition frequency	10 Hz (single pulse)	10 Hz (single pulse)	1 kHz
Deposited energy	2.5 - 3.5 mJ per pulse	2.5 mJ per pulse	2.5 mJ (0 – 20 ns) 3.0 mJ (0 – 100 ns)
Maximum ΔV	8.5 kV	5.5 kV	8 kV
Pressure	5.8 kPa – 0.1 MPa	0.1 MPa	0.1 MPa
Gas	Ambient air	Ambient air (with 1.6% of H_2)	Ambient air (with 3.7% of H_2)

The experimental parameters used in the present study are summarized in Table 2. The experimental parameters of our previous work, performed in a single pulse regime, are also compared.

3. Experimental results

In Section 3.a, the measurements of the electron number density using the Stark broadening of H_α, at $\lambda = 656$ nm, and N^+, at $\lambda = 500$ nm, are described. Each line covers a different range of ionization degrees and their overlap serves as a validation of our procedure. In Section 3.b, the discharge radius is measured using the calibrated Optical Emission Spectroscopy (OES) of N^+ and O^+ recorded near $\lambda = 500$ nm. In Section 3.c, the electron number density is measured via the electron continuum emission. The measurements are spatially resolved along the interelectrode gap. In Section 3.d, we compare the results obtained with the different methods in the region near the cathode, which is the location where the transition to a fully ionized plasma is the fastest.

a. Stark broadening of H_α

A review of line broadening for several atoms and ions, including N^+, O^+, and H_α, was presented in our previous work [25]. In this Section, the primary sources of broadening of the H_α transition are calculated, showing that Stark broadening is the dominant mechanism. For the N^+ lines, the methods employed in this study are the same as in [25] and are not described here.

The electron number density can be accurately measured using the Stark broadening of the H_α line at 656 nm. The Half-Width at Half Maximum (HWHM) of H_α results from several broadening mechanisms: Doppler, resonant, natural, Van der Waals, Stark, and instrumental [25,57,58]. In the following, we estimate the non-Stark contributions to the HWHM of the H_α line and show that they are negligible. The broadening formulas used in the present work were initially developed by Griem [57] and simplified for H_β in [58]. The work of Ref. [58] was recently improved and extended to H_α, H_β, O, N, O^+, and N^+ [25]. In the following, the gas transformation is assumed to be isochoric with an initial ambient number density of 2.7×10^{19} cm^{-3}. The gas temperature varies from 300 K (initial condition) to ~ 30,000 K (fully ionized plasma), which induces moderate changes in **the Doppler** HWHM. The number density of atomic hydrogen is estimated to be below 10^{15} cm^{-3}, resulting in negligible **resonant broadening** (HWHM < 1 pm). **Natural broadening** is also negligible. **Van der Waals broadening** results from the perturbation of the H_α transition by non-hydrogenic particles (N_2, O_2, O, N, O^+, and N^+). The sum of all the contributions is given in Eq. 2, where N is the total gas density, T_{gas} the gas temperature, and x_{pert} the perturber mole fraction. The coefficients γ_{pert} are specific to each transition–perturber couple and are calculated in Ref. [25].

$$\Delta\lambda_{Van\ der\ Waals}[nm] = \frac{N}{2.7\times10^{19}\ [\mathrm{cm^{-3}}]}\left(\frac{T_{gas}}{273\ [\mathrm{K}]}\right)^{0.3}\sum_{pert}\left(\frac{\gamma_{pert}}{100}x_{pert}\right) \qquad \text{Eq. 2}$$

The sum in Eq. 2 can be simplified using γ_{mean} defined in Eq. 3.

$$\gamma_{mean} = \sum_{pert}\left(x_{pert}\gamma_{pert}\right) \qquad \text{Eq. 3}$$

In Table 3, the value of γ_{mean} is calculated in air. During the thermal spark formation, the gas composition varies from N_2:O_2 at 300 K, to N:O at 20,000 K, and finally N^+:O^+:e^- at 40,000 K. For these compositions, the Van der Waals HWHM varies from 34 to 267 pm. For comparison, when the plasma is partially ionized at 20,000 K, a Stark HWHM of 34 pm corresponds to $n_e \sim 10^{14}$ cm^{-3}, which is well below our sensitivity limit. When the gas is fully ionized and T = 40,000 K, a Stark broadening of 34 pm would correspond to an electron number density of 3×10^{16} cm^{-3}, which is three orders of magnitude lower than the measured electron number density. The Van der Waals broadening is therefore negligible compared to the Stark broadening.

Table 3 Estimated γ_{mean} coefficient and Van der Waals broadening HWHM of the H_α line in ambient air at 300 K, dissociated air at 20,000 K, and fully ionized air at 40,000 K.

Composition	γ_{mean}	T (K)	N (cm^{-3})	$\Delta\lambda_{VdW}$ (pm)
N_2 / O_2	3.36	300	2.7×10^{19}	34
N / O	3.64	20,000	5.4×10^{19}	150
N^+ / O^+	3.26	40,000	5.4×10^{19}	267

The instrumental broadening for a given spectrometer focal length mainly depends on the spectrometer slit opening and its grating. We used two gratings in this study to follow the variations of the H_α HWHM from 0.1 nm to 20 nm. The corresponding instrumental HWHM is given in Table 4. A typical example of the H_α line fit is shown in Figure 4. The H_α width uncertainty is about ±20%, which leads to a 30% uncertainty on the n_e measured with this technique.

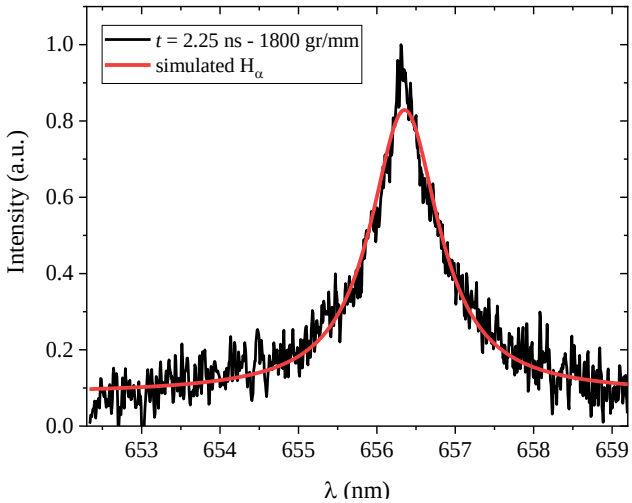

Figure 4 Fit of the Hα line at *t* = 2.25 ns (1800-gr/mm grating).

The **Stark broadening** HWHM can be calculated[2] with Eq. 4 [59,60].

$$\frac{n_e}{10^{17}\ \mathrm{cm^{-3}}} = \left(\frac{\Delta\lambda_{\mathrm{Stark,H\alpha}}}{0.549\ \mathrm{nm}}\right)^{1.47134} \qquad \text{Eq. 4}$$

In this work, Stark broadening measurements are performed during the high-voltage pulse. In Ref. [61], it was shown that the applied electric field could have an impact on the Stark broadening. In that case, the width of the spectral line would be related to the current density instead of the electron number density. In Ref. [61], expressions are derived for the Stark broadening of H_α and H_β generated by the sum of two fields:

- A microscopic field, arising from the presence of ions and electrons in plasma. *This is the typical Stark broadening effect.*
- A macroscopic field applied in one direction during the experiment. *This field can interfere with the Stark broadening.*

According to Bastien & Marode [61], the H_β Stark broadening is mainly due to the shifting of intense external lines caused by the static ions' microfield. Thus, the addition of an external field has an impact on the H_β Stark broadening. On the other hand, Bastien & Marode showed that the addition of an external field has a weak impact on the H_α lineshape. For instance, at $n_e = 10^{17}$ cm^{-3} and T_e = 10,000 K, the Stark HWHM of H_α remains independent of the applied field up to at least 12 kV·mm^{-1} (four times the Holtsmark field, see Table 1 of [61]). In our experiments, the maximum applied field is 6.7 kV·mm^{-1} when $n_e \sim 10^{17}$ cm^{-3}. Therefore, the applied field does not influence our Stark broadening measurements of H_α during the pulse.

To summarize, the Doppler, resonant, and Van der Waals HWHM are negligible or smaller than the Stark broadening width, see Table 4. Their contribution is however included in the post-processing of the OES spectra.

Table 4 Estimation of the Hα line HWHM (in pm) for the present conditions based on the formula given in Ref. [25]**. See also Table 3 for the estimation of the Van der Waals HWHM.**

Time (ns)	T_{gas} (K)	Doppler (pm)	Resonant (pm)	Van der Waals (pm)	Instrumental broadening (pm)	Stark (pm)
0 – 4	300 – 3000	4 - 12	<1	< 34	48 (1800 gr·mm^{-1})	100 – 600

[2] The relation given initially by Gigosos *et al.* [59] must be corrected by a factor 2 as noted by Konjević *et al.* [60].

3 – 20	3000 – 30,000	12 - 38	<1	< 267	342 (300 gr·mm^{-1})	600 – 23,000

b. Discharge radius measurement using N^+ and O^+ path-integrated number density

In this subsection, the results of the intensity-calibrated OES near 500 nm are presented and employed to measure the discharge optical diameter. In the work of Shcherbanev *et al.* [42], it was reported that the emission of filamentary SDBD was the sum of two concentric channels. In their case, the intense N^+ and continuum spectral features were emitted from the central core, whereas a weaker N_2 emission originated from the outer shell. Shcherbanev *et al.* reported a central core Full Width at Half Maximum (FWHM) of 18 ± 2 µm. In a configuration similar to ours, Orrière measured the FWHM of a thermal spark [47]. He found an FWHM of 50 µm for a 6-kV discharge of 20 ns applied across a 1-mm gap between the electrodes[3]. However, no spectral filter was used; therefore, the measurement of Orrière *et al.* is an upper bound of their thermal spark diameter. In a 25-kV discharge of 40 ns at ambient conditions, Parkevich *et al.* [36] used interferometry to show that their discharge was composed of several fully ionized filaments, 10 – 50 µm in diameter. A recent study by Parkevitch and Khirianova [62] suggests that the formation of several smaller propagating filaments (instead of a single one) occurs above a current threshold of 40 – 100 A. Finally, Lo *et al.* clearly observed a constriction of the discharge channel during the transition to the thermal spark in a microsecond pulsed discharge in air [28].

In the present study, the plasma column diameter is estimated by focusing the discharge image on the CCD with a magnification factor of 2 and employing a 10-nm bandpass filter centered at 480 nm (Hard Coated OD 4.0 10-nm Bandpass Filter, Edmund Optics). An accurate measurement is challenging with our present setup because of the shot-to-shot spatial displacement of the discharge (~10 µm) and because the column width is comparable with the pixel width, which could result in pixel bleeding. Nevertheless, the CCD images provide a first-order estimate of the plasma diameter of the order or less than the pixel resolution, *i.e.* Δl = 15 µm. This value is similar to the measurements of Shcherbanev *et al.*, Orrière, and Parkevich *et al.*

At T ~ 30,000 K, the plasma reaches complete ionization and hence thermal and chemical equilibrium [25]. At these temperatures, after an isochoric transformation, the plasma is mainly composed of electrons (50%), and ions N^+ (40%) and O^+ (10%) [63]. The electron number density was determined as described in Section 3.a. Thus, because the plasma is neutral, the number density of the ions (N^+ and O^+) is known and equal to n_e. The spectral emissivity of a uniform emission spectrum due to a given transition at λ [nm] is a function of the upper state ion number density, n_{ion}[cm^{-3}], the photon energy (hc/λ), the transition upper state energy and degeneracy, ε_u [J] and g_u, the temperature, T [K], the partition function, $Q(T)$, the transition Einstein coefficient, A [s^{-1}], the plasma optical diameter Δl [m^{-1}], the absorption coefficient k [m^{-1}], and the broadening function, ϕ [nm^{-1}], see Eq. 5 [64].

$$\varepsilon[\mathrm{W{\cdot}cm^{-3}{\cdot}sr^{-1}{\cdot}nm^{-1}}] = n_{ion}\frac{g_u \exp(-\varepsilon_u/kT)}{Q(T)}\frac{A}{4\pi}\frac{hc}{\lambda}\,\phi\frac{k}{1-\exp(-k\Delta l)} \qquad \text{Eq. 5}$$

Thus, the knowledge of the calibrated intensity spectrum of a given line of N^+ or O^+ and the electron density can provide a direct measurement of the discharge diameter, Δl.

[3] For a 2-kV pulse across 200-µm gap, Orriere measured a FWHM of 40 µm.

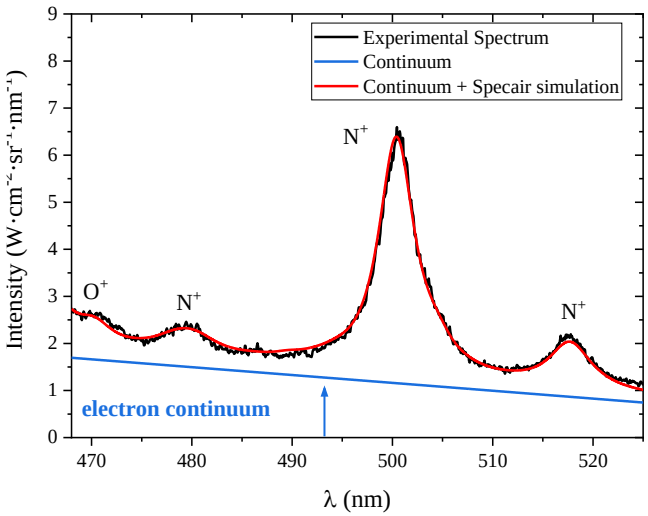

Figure 5 Fit of the N^+ and O^+ emission near the cathode at *t* = 9.75 ns. The continuum emission is approximated by a linear function (in blue) and the N^+ and O^+ emission is calculated by Specair (in red). The N^+ and O^+ lines are calculated, accounting for self-absorption.

A typical spectrum is shown in Figure 5. The spectrum is fitted using an in-house extension of Specair [58,65] and accounting for self-absorption. For O^+ and N^+ lines, the Stark line broadening dominates and the lineshape fit provides another measurement of n_e. The uncertainty on the Stark broadening fitting (and n_e determination) is below 20%. The continuum radiation (assumed to be linear) is subtracted and studied in Section 3.c. All electronic states of the ions are assumed to follow a Boltzmann distribution at T_e. The measured electronic temperature (T_e = 35,000 K) corresponds to values usually reported in the thermal spark literature [25,28,32]. The accuracy of the T_e measurements is ± 5%, implying that the path-integrated radiance is at best 30% accurate.

Because the plasma is globally neutral, we have $n_e = n_{N+} + n_{O+}$, where n_e is taken from the N^+ Stark broadening. The inferred plasma diameter evolution using this assumption and Eq. 5 is shown in Figure 6. This method theoretically offers a micrometer resolution and allows tracking the growth of the filament with sub-nanosecond resolution during its development. Initially, the thermal spark diameter is only about 1 µm, then grows to an asymptotic value of about 10 µm after about 20 ns. These filament diameters (about 10 µm at the end of the discharge pulse) are consistent with those reported for SDBD, i.e. 18 µm, during the transition to a fully ionized plasma [42]. Also, the estimate based on CCD imaging (15 µm) is within the error bars. This time-resolved optical diameter is used in the next section to process the electron continuum measurements.

We now discuss the potential effects arising due to such small diameters where the magnetic pressure could play a role. Assuming an isochoric heating from 300 to 30,000 K, complete dissociation and ionization, then the kinetic pressure is P_k ~ 400 atm. The magnetic pressure, P_m, can be estimated from Eq. 6, where $\mu_0 = 4\pi \cdot 10^{-7}$ H·m^{-1} is the magnetic permeability and *B* the tangential magnetic field.

$$P_m = \frac{B^2}{2\mu_0} \qquad \text{Eq. 6}$$

The tangential magnetic field on the filament boundary can be approximated by the magnetic field generated by an infinitely thin straight wire. Using $B = \mu_0 I / 2\pi R_f$, where I is the electrical current, and R_f is the filament radius, the magnetic pressure is given by Eq. 7 [42].

$$P_m = 0.157\left(\frac{I[\mathrm{A}]}{R_f[\mu\mathrm{m}]}\right)^2 [\mathrm{atm}] \qquad \text{Eq. 7}$$

Using typical values corresponding to the present case, I = 200 A and R_f = 1 µm, we obtain P_m = 6300 atm ~ 10 P_k. Thus, a z-pinch effect is likely to reduce the discharge diameter and prevent its expansion until the end of the current pulse. For t > 7 ns, the current decreases (see later in Figure 9), which decreases the magnetic pressure and allows the diameter to increase.

No explanation is currently provided in the literature for the origin of micrometer filaments. The theory of Raizer [1] on leader propagation does not explain this phenomenon. As n_e increases near the cathode, the cathode sheath size and the electron collision cross-section decrease. As a consequence, the cathode sheath becomes collisionless and runaway electrons can be formed [66–68]. These highly energetic electrons enter the partially ionized zone and could leave a trail of seed electrons behind, which could trigger the transition to a fully ionized region. This potential explanation needs validation and could be simulated in air by combining the approach of Levko and Raja [66,67] with the kinetic mechanism presented in the next section.

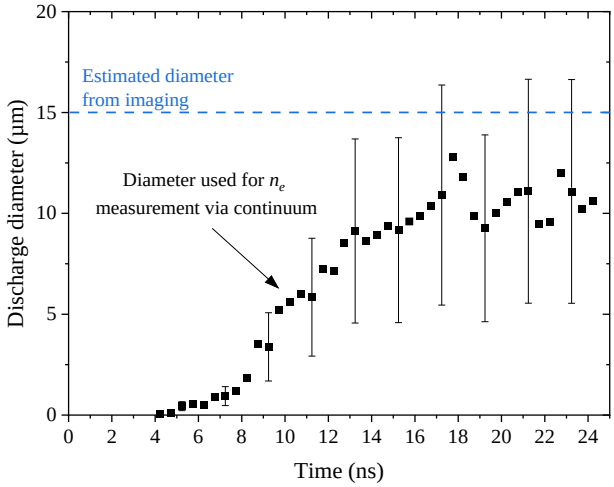

Figure 6 Discharge optical diameter evolution deduced from the ionic line radiation, and comparison with the diameter estimated using CCD imaging (dashed blue line).

c. Continuum radiation of electrons

This Section describes another method for measuring the electron number density, this time using the electron continuum emission. As shown in several works, continuum radiation can be significant in laser-induced plasmas [69], DBD discharges [42], or pin-to-pin nanosecond discharges [70]. Recently, laser absorption by the electron continuum was employed to measure the ionization degree of a fully ionized plasma [71].

The electron continuum emission results from the free-free radiation (also called Bremsstrahlung) and the free-bound radiation (also called recombination continuum). The continuum emission coefficient is given in Eq. 8, where n_e and n_i are the electron and ion number densities, Z_i the ion charge, T_e the electron temperature, ξ the free-bound Gaunt factor, and G the free-free Gaunt factor [72].

$$\varepsilon_c(\lambda, T_e, n_e) = C_8 Z_i \frac{n_e n_i}{\lambda^2\sqrt{T_e}}[\xi(1-e^{-u}) + Ge^{-u}] \qquad \text{Eq. 8}$$

If several types of ions are present in the mixture, the total continuum radiation will be a sum over Z_i, i being the ion species. In the present case, we consider that N^+ is the dominant ion and Z_i = 1. If the plasma is mainly composed of

neutral atoms, another formulation must be used [73,74]. The C_8 constant can be determined with Eq. 9, where e is the electron charge, k_b the Boltzmann constant, c the speed of light, and m_e the electron mass.

$$C_8 = \frac{16\pi e^6}{3c^2\sqrt{6\pi m_e^3 k_b}} = 1.63 \times 10^{-34} \left[\mathrm{W{\cdot}m^3{\cdot}nm{\cdot}K^{0.5}{\cdot}sr^{-1}}\right] \quad \text{Eq. 9}$$

The dimensionless variable u is defined in Eq. 10, where h is the Planck constant, k_b the Boltzmann constant, c the speed of light and λ the wavelength.

$$u = \frac{hc}{\lambda k_b T_e} \quad \text{Eq. 10}$$

The free-free Gaunt factor of N^+ (and O^+) at λ = 500 nm varies from G = 1.08 to G = 1.1 for T in the range 32,000 – 42,000 K, interpolating[4] the results of [75]. The free-bound Gaunt factor should be averaged on the atom's final states (*i.e.* after the electron has recombined with the ion). The free-bound Gaunt factor at λ = 500 nm (= 0.18 Ry) ranges between ξ = 0.8 and ξ = 1.2 depending on the final bound state (see the values calculated for any ions in Table 1 of Ref. [76]). Here we assume ξ = 1 and G = 1.09. These coefficients are considered to be accurate[5] within 10%. Assuming $n_e = n_i$, we obtain n_e [m^{-3}] as a function of λ [nm], the volumetric emission coefficient ε_c [$W{\cdot}m^{-3}{\cdot}sr^{-1}{\cdot}nm^{-1}$], and T_e [K], see [72]:

$$n_e^2 = \frac{\lambda^2\sqrt{T_e}}{C_8}\frac{1}{\xi(1-e^{-u}) + Ge^{-u}}\,\varepsilon_c \quad \text{Eq. 11}$$

Solving the radiative transport equation [64], the spectral emissivity ε_c is related to the continuum intensity I_c [$W{\cdot}m^{-2}{\cdot}sr^{-1}{\cdot}nm^{-1}$], the absorption coefficient k [m^{-1}], and the plasma width Δl [m] as follows:

$$I_c = \varepsilon_c \frac{1-\exp(-k\Delta l)}{k} \quad \text{Eq. 12}$$

The absorption coefficient, k, is the sum of the continuum and bound-bound absorption, k_{bb} and k_c, respectively. In a worst-case scenario, we assume that the absorption coefficient across the entire spectrum is equal to the bound-bound contribution, *i.e.* $k \sim k_{bb}$. For a plasma diameter of 15 µm and $n_e = n_{N^+} = 10^{19}$ cm^{-3}, we calculated with Specair that $k_{bb}\Delta l < 0.5$ between 460 and 530 nm. Based on this estimation, the plasma is optically thin, *i.e.* $I_c \approx \varepsilon_c \Delta l$. This approximation leads to an overestimation of ε_c by 40% at most, which is acceptable, as shown in the next paragraph. Finally, Eq. 11 can be further simplified as given by Eq. 13, where n_e [m^{-3}] is a function of Δl [m] the plasma width, I_c [$W{\cdot}m^{-2}{\cdot}sr^{-1}{\cdot}nm^{-1}$] the continuum intensity, T_e [K] the electron temperature, and λ [nm] the wavelength of observation.

$$n_e = \left(\frac{\lambda^2\sqrt{T_e}}{C_8}\frac{1}{\xi(1-e^{-u}) + Ge^{-u}}\frac{I_c}{\Delta l}\right)^{\frac{1}{2}} \quad \text{Eq. 13}$$

Thanks to the power 1/2 on the right-hand side of Eq. 13, the impact on the electron number density of the uncertainty on the measured intensity I_c is halved. The uncertainty on T_e is about 10%. The free-free and free-bound coefficients vary slowly with T_e and, in this case, are known within ±10%. The intensity calibration of the absolute spectrum is accurate within about ±20%. Considering the thin plasma assumption, the maximum uncertainty on ε_c is +20% and -60%. The plasma thickness, Δl, is estimated to be accurate within 30%. Therefore, after propagation of the uncertainties through quadrature summation, the n_e deduced from the continuum emission is found to be accurate within -70% and +40%.

[4] We used the ChiantiPy Python package [118,119] at https://github.com/chianti-atomic/ChiantiPy.

5 If needed, a more precise value could be obtained using the summation performed by ChiantiPy with the values of [120]. As described later, the dominant uncertainty comes from on the plasma thickness and the Gaunt factors uncertainty is unimportant.

d. Comparison of the electron density measurements

Electron number densities measured with the three techniques described above are compared in Figure 7. The H_α line measurements are performed using two gratings, with an overlap between the acquisitions to ensure data reproducibility. From t = 1.25 ns to t = 8 ns, n_e increases from 10^{16} to 3×10^{19} cm^{-3}. The steep increase of the electron number density (over a decade) at t = 4 ns corresponds to the filament formation. For t = 4 – 6 ns, the continuum emission measurements (triangles) are slightly above those obtained from H_α Stark broadening (circles), whereas the Stark broadening of N^+/O^+ (squares) slightly overestimates the H_α Stark broadening measurements. For t > 6 ns, the measurements from the three techniques are in excellent agreement within the error bars. For t > 10 ns, the electron density slowly decays to 5×10^{18} cm^{-3} at 23 ns due to the isentropic expansion of the plasma channel [25,28]. These spectroscopic measurements are compared to those performed by Orrière and Pai [32] in a nanosecond discharge generated in a 200-µm gap via the estimation of the gap conductivity.

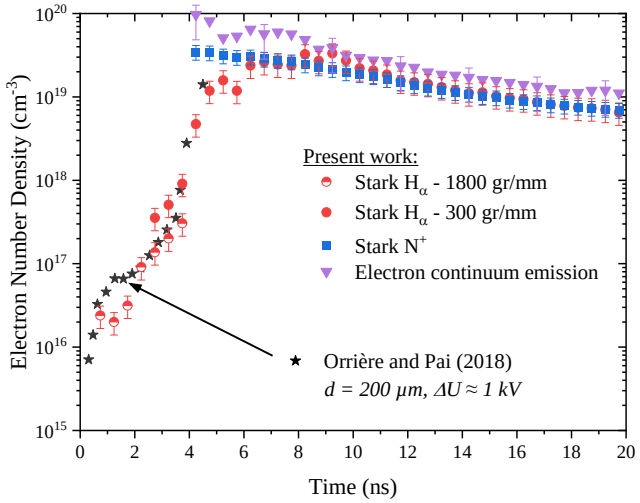

Figure 7 Evolution of the electron number density near the cathode measured with Stark broadening of H_α (red circles), Stark broadening of N^+ (blue squares), and continuum radiation (purple triangles). We assumed an optically thin plasma for continuum radiation interpretation only (uncertainty propagated in the error bars). Our measurements are compared to those of Orrière and Pai, see Figure 6 of [32].

4. Kinetic model of the thermal sparks

a. Introduction and numerical setup

In this Section, 0-D numerical simulations of plasma kinetics as a function of the reduced electric field are performed using ZDPlasKin [78]. We assume an isochoric transformation of the plasma, which is typically the case for nanosecond discharges. The heat capacity ratio is considered constant, c_p/c_v = 1.4, because it has a negligible effect on the speed of ionization calculated in this work. The Electron Energy Distribution Function (EEDF) is calculated by solving the Boltzmann equation accounting for the mixture composition at each timestep with BOLSIG+ [79,80], using cross-sections of electron reactions taken mostly from the LXCat database [81–85]. BOLSIG+ was not tested by its developers above an ionization fraction of 1% and we did not modify the solver. Nevertheless, it was shown in our previous work that, for an ionization fraction above 1%, BOLSIG+ gives the same results as a kinetic simulation assuming a Boltzmann EEDF, see Figure 11 of [26].

Several kinetic mechanisms for low-temperature plasmas are available in the literature [50,53,54] and could have been used as a baseline. For instance, the reaction set of Capitelli *et al.* was employed in our previous work on the thermal spark [86]. However, these mechanisms include hundreds of reactions, such as the formation of negative ions and N_yO_x with (x, y) ≥ 2, which are unnecessary to describe the thermal spark formation. Instead, in this work, we employ a simplified 38-reaction set from Laux *et al.* [8], supplemented with reactions taken from Popov [23] and Shcherbanev *et al.* [42]. The reaction set of Laux *et al.* is adequate because only the essential reactions and species driving the ionization and recombination of plasma discharges in air are included. The selected reactions taken from Popov include the ultrafast heating mechanism, whereas those from Shcherbanev *et al.* [42] account for the dissociation and ionization of N_2 excited states [87]. The originality of the present mechanism is the addition of the excitation and ionization of N and O electronically excited states [88–90]. This new mechanism includes N_2, O_2, NO, N, O, N_2^+, O_2^+, NO^+, N^+, O^+, N^{++}, and O^{++}. A simplified representation of the kinetics and the main sources employed in this work is given in Figure 8.

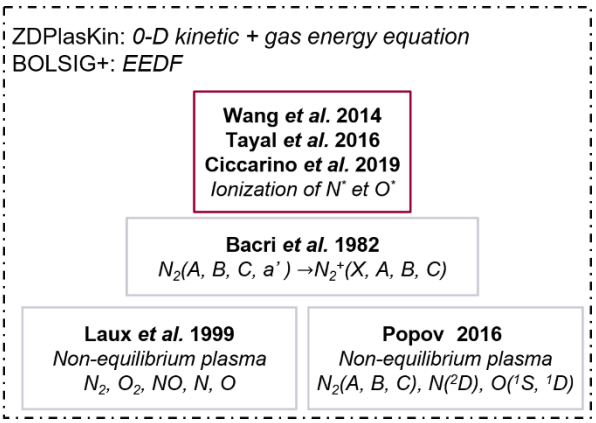

Figure 8 Overview of the reactions included in the present mechanism [8,23,42,87–90]**.**

b. Detailed balance

The reverse rates are computed in these simulations via detailed balance [91,92]. Let us define Reac. 1 involving four species: A, B, C, and D.

$$A + B \leftrightarrow C + D \qquad \text{Reac. 1}$$

If the forward rate coefficient of Reac. 1, k_f, is known, then the reverse rate coefficient, k_r, can be computed using Eq. 14, where Z_X is the partition function of species or pseudo-species X.

$$\frac{k_f}{k_r} = \frac{Z_C Z_D}{Z_A Z_B}(T) \qquad \text{Eq. 14}$$

If the collision partners are heavy particles, $T = T_{gas}$ in Eq. 14. However, if one electron is involved[6], then $T = T_e$. For instance, in the case of ionization/recombination of atomic nitrogen N(^{4}S), see (R76), the detailed balance is equivalent to the Saha formula (Eq. 15), where m_e is the electron mass, k_b the Boltzmann constant, T_e the electron temperature, h the Planck constant, g_X the degeneracy of the species or pseudo-species X, I the ionization energy of N(^{4}S), and $k_{f,i}$ the ionization rate computed with BOLSIG+.

[6] A particular treatment must be applied for three-body reactions involving two heavies and one electron but does not apply to this work [121].

$$k_{r,i} = \frac{1}{2}\left(\frac{2\pi m_e k_b T_e}{h^2}\right)^{-\frac{3}{2}} \frac{g_{\mathrm{N}(^4\mathrm{S})}}{g_{\mathrm{N}^+}} \exp\left(\frac{\mathrm{I}}{k_b T_e}\right) k_{f,i} \qquad \text{Eq. 15}$$

The first term in Eq. 15 is the inverse of the electron partition function and the factor 1/2 accounts for the electron spin. The Saha formula is exact if the EEDF is a Maxwellian (the use of T_e requires to have a Maxwellian EEDF).

c. List of reactions

This subsection provides the list of reactions and the motivation behind their selection.

Table 5 The baseline kinetic mechanism used in this work is mainly taken from [8]**. The forward reaction coefficients are given, with their dependence on either the gas temperature or the electron temperature. The backward reaction rates are always calculated by detailed balance. The star symbol (*) refers to the forward reaction rates identical to those reported in Table 1 of** [8]**.**

Reaction & Temperature dependence			$k_f = A\,T^b \exp(-E/RT)$			Ref.
		k_f k_r	A ($cm^3\ s^{-1}$)	b	E/R (K)	
	O_2, NO, N_2 Dissociation / Recombination [8]					
(R1)	$O_2 + N_2 \leftrightarrow 2O + N_2$	T_g T_g	$3.32\ 10^{-3}$	-1.5	59,500	[93] *
(R2)	$O_2 + O_2 \leftrightarrow 2O + O_2$	T_g T_g	$3.32\ 10^{-3}$	-1.5	59,500	[93] *
(R3)	$O_2 + NO \leftrightarrow 2O + NO$	T_g T_g	$3.32\ 10^{-3}$	-1.5	59,500	[93] *
(R4)	$O_2 + N \leftrightarrow 2O + N$	T_g T_g	$1.66\ 10^{-2}$	-1.5	59,500	[93] *
(R5)	$O_2 + O \leftrightarrow 2O + O$	T_g T_g	$1.66\ 10^{-2}$	-1.5	59,500	[93] *
(R6)	$O_2 + e \leftrightarrow O + O(^3P) + e$	T_e T_e	BOLSIG+			[94]
(R7)	$O_2 + e \leftrightarrow O + O(^1S) + e$	T_e T_e	BOLSIG+			[94]
(R8)	$NO + N_2 \leftrightarrow N + O + N_2$	T_g T_g	$8.30\ 10^{-9}$	0.0	75,500	[93] *
(R9)	$NO + O_2 \leftrightarrow N + O + O_2$	T_g T_g	$8.30\ 10^{-9}$	0.0	75,500	[93] *
(R10)	$NO + NO \leftrightarrow N + O + NO$	T_g T_g	$1.83\ 10^{-7}$	0.0	75,500	[93] *
(R11)	$NO + N \leftrightarrow N + O + N$	T_g T_g	$1.83\ 10^{-7}$	0.0	75,500	[93] *
(R12)	$NO + O \leftrightarrow N + O + O$	T_g T_g	$1.83\ 10^{-7}$	0.0	75,500	[93] *
(R13)	$N_2 + N_2 \leftrightarrow 2N + N_2$	T_g T_g	$1.16\ 10^{-2}$	-1.6	113,200	[93] *
(R14)	$N_2 + O_2 \leftrightarrow 2N + O_2$	T_g T_g	$1.16\ 10^{-2}$	-1.6	113,200	[93] *
(R15)	$N_2 + NO \leftrightarrow 2N + NO$	T_g T_g	$1.16\ 10^{-2}$	-1.6	113,200	[93] *
(R16)	$N_2 + N \leftrightarrow 2N + N$	T_g T_g	$4.98\ 10^{-2}$	-1.6	113,200	[93] *
(R17)	$N_2 + O \leftrightarrow 2N + O$	T_g T_g	$4.98\ 10^{-2}$	-1.6	113,200	[93] *
	Zeldovich reactions [8]					
(R18)	$N_2 + O \leftrightarrow NO + N$	T_g T_g	$1.06\ 10^{-6}$	-1.0	38,400	[93] *
(R19)	$NO + O \leftrightarrow O_2 + N$	T_g T_g	$1.39\ 10^{-11}$	0.0	19,400	[93] *
	Associative ionization / Dissociative recombination [8]					
(R20)	$N + O \leftrightarrow NO^+ + e$	T_g T_e	$1.46\ 10^{-15}$	1.0	31,900	[93]
(R21)	$N + N \leftrightarrow N_2^+ + e$	T_g T_e	$9.97\ 10^{-17}$	1.5	67,500	[93]
(R22)	$O + O \leftrightarrow O_2^+ + e$	T_g T_e	$1.18\ 10^{-21}$	2.7	80,600	[93]
	Electron Impact Ionization of O_2 and NO [8]					
(R23)	$O_2 + e \leftrightarrow O_2^+ + 2e$	T_e T_e	BOLSIG+			[95]
(R24)	$O_2 + e \leftrightarrow O^+ + O + 2e$	T_e T_e	BOLSIG+			[95]
(R25)	$NO + e \leftrightarrow NO^+ + 2e$	T_e T_e	BOLSIG+			[96]
(R26)	$NO + e \leftrightarrow N + O^+ + 2e$	T_e T_e	BOLSIG+			[96]
(R27)	$NO + e \leftrightarrow O + N^+ + 2e$	T_e T_e	BOLSIG+			[96]

	Charge Exchange [8]					
(R28)	$N^+ + N_2 \leftrightarrow N + N_2^+$	T_g T_g	$1.66\ 10^{-12}$	0.5	12,000	[93]
(R29)	$NO^+ + O \leftrightarrow N^+ + O_2$	T_g T_g	$1.66\ 10^{-12}$	0.5	77,200	[93] *
(R30)	$NO + O^+ \leftrightarrow N^+ + O_2$	T_g T_g	$2.32\ 10^{-19}$	1.9	26,600	[93]
(R31)	$NO^+ + N \leftrightarrow N_2 + O^+$	T_g T_g	$5.65\ 10^{-11}$	-1.08	12,800	[93]
(R32)	$O^+ + N_2 \leftrightarrow N_2^+ + O$	T_g T_g	$1.49\ 10^{-12}$	0.36	22,800	[93]
(R33)	$NO^+ + N \leftrightarrow N_2^+ + O$	T_g T_g	$1.20\ 10^{-10}$	0.0	35,500	[93] *
(R34)	$O_2^+ + N \leftrightarrow N^+ + O_2$	T_g T_g	$1.44\ 10^{-10}$	0.14	28,600	[93]
(R35)	$O_2^+ + N_2 \leftrightarrow N_2^+ + O_2$	T_g T_g	$1.64\ 10^{-11}$	0.0	40,700	[93]
(R36)	$NO^+ + O_2 \leftrightarrow NO + O_2^+$	T_g T_g	$3.99\ 10^{-11}$	0.41	32,600	[93]
(R37)	$NO^+ + O \leftrightarrow N + O_2^+$	T_g T_g	$1.20\ 10^{-11}$	0.29	48,600	[93]

Most of the reactions used by Laux *et al.* are taken from [93,97]. However, some reaction rate coefficients in [97] are calculated for T_{gas} = 2000 K, which is unsuitable for the present work. Therefore, the reaction rates calculated in [93] are replaced with calculations performed using BOLSIG+ with the cross-sections specified in Table 5. In the case of (R28), $N^+ + N_2 \leftrightarrow N + N_2^+$, the rate constant is taken from [93]. Note that some of the rate coefficients of charge exchange reactions were rounded off in Table 1 of [8], but the exact values were used in their simulation and ours.

The ionization of NO by electron impact was initially limited to (R25), $NO + e \leftrightarrow NO^+ + 2e$, in [8]. We added here the formation of O^+ and N^+, (R26) and (R27) [96]. To our knowledge, the cross-section of NO dissociation by electron impact is not available in the literature [96]. BOLSIG+ computes the rate of O_2 dissociation by electron impact based on the cross-sections[7] provided in [94]. In this model, the N_2 dissociation and ionization by electron-impact are state-specific and more details are given in Table 6. The heating due to NO^+, N_2^+, and O_2^+ dissociative recombination was found to have a minor impact on the temperature increase (less than 50 K) [42].

For electron-heavy reactions, the rate constant is a function of the electron temperature. For heavy-heavy reactions, the rate constant is a function of the gas temperature. As discussed in Section 4.b this is critical for associative ionization and dissociative recombination, whose rate constants depend on T_g and T_e, respectively. Finally, the dissociative recombination of N_2^+, (R21), is calculated with detailed balance using Park's rate of associative ionization. An alternative method, not employed in this study, would have been to take the cross-sections calculated by [87] or measured by [98].

Table 6 Additional set of reactions calculated with BOLSIG+.

Reaction		Cross-section
	Electronic Excitation of N_2	
(R37)	$N_2 + e \leftrightarrow N_2(Y) + e$ Y = A, B, C, a'	[99]
(R38)	$N_2(Z) + e \leftrightarrow N_2(Y) + e$ Z = A, B, C, a' Y = B, C, a'	[87]
	Ionization and dissociation of N_2	
(R39)	$N_2(X) + e \leftrightarrow N_2^+(Y) + 2e$ Y = X, B	[100]
(R40)	$N_2(X) + e \leftrightarrow N_2^+(Y) + 2e$ Y = A, C	[87]
(R41)	$N_2(Z) + e \leftrightarrow N_2^+(Y) + 2e$	[87]

[7] Available in the LXCat *Phelps database* or the LXCat *LISBON-IST database*

	Z = A, B, C, a’	
	Y = X, A, B, C	
(R42)	$N_2(X) + e \leftrightarrow N + N(^2D) + e$	[83,101]
(R43)	$N_2(Z) + e \leftrightarrow N + N(^2D) + e$	[87]
	Z = A, B, a’, C	
	Electronic transitions of N_2^+	
(R44)	$N_2^+(Z) + e \leftrightarrow N_2^+(Y) + e$	
	Z = X, A, B, C	[87]
	Y = X, A, B, C	

The cross-sections of the electronic excitation of $N_2(X)$ to higher excited states were measured by Cartwright *et al.* [102] and later renormalized by Trajmar *et al.* [103]. Usually, these cross-sections are linked to the *LXCaT Phelps Database* [104]. In our kinetic simulations, the cross-section of electron-impact excitation of N_2 to $N_2(A^3\Sigma_u^+)$ is the sum of the cross-sections to the $N_2(A, v')$ levels taken from [99]. The $N_2(B^3\Pi_g, B^3\Sigma_u^-, W^3\Delta_u)$ states are lumped together in the $N_2(B)$ state, using the renormalized cross-sections of [102]. This is also the case for $N_2(C)$, which is the sum of $N_2(C^3\Pi_u, E^3\Sigma_g^+)$ states. The $N_2(a'^1\Sigma_u^-, a^1\Pi_g, w^1\Delta_u)$ singlet states are lumped together in the $N_2(a')$ state. This grouping was initially proposed in [53] and used in the kinetic mechanism[8] of [51]. If further refinements of these reactions were needed, one should focus on distinguishing $N_2(a'^1\Sigma_u^-)$ and $N_2(a^1\Pi_g)$ because their dissociation cross-sections differ by one order of magnitude.

The electronic excitation of N_2(A, B, C, a’) by electron impact as well as the transitions between the N_2^+(X, A, B, C) states by electron impact are taken from [87]. The ionization cross-sections of $N_2(X)$ to N_2^+(X, B), (R39), were estimated in [100] based on the (normalized) measurement of Cartwright *et al.* and the recommendations of Itikawa[9]. The ionization cross-sections of N_2(A, B, a’, C), (R41), are taken from [87]. The dissociation cross-section of N_2 ground state, (R42), is taken from [83,101], whereas the dissociation cross-sections of the electronically excited states, (R43), are from [87]. In electron-impact dissociation of any electronic state of N_2, the fragments are $N(^4S)$ and $N(^2D)$ [83,101] . Reactions involving the excited electronic states of NO and O_2 are neglected in this work because these species are not dominant in these air plasmas[10].

[8] Available online: www.zdplaskin.laplace.univ-tlse.fr/author/sergey-pancheshnyi/index.html

[9] We note however that these ionization cross-sections include the dissociative ionization cross-sections. The impact of this approximation is limited in the present case because $N_2(X)$ ionization only drives the partial ionization phase.

[10] If O_2 excited states were to be included in a simulation, we recommend using the cross-sections of the LXCat *Phelps database*, see [51]. It was argued, however, that these states have a minor impact on the chemistry [50]. For NO electronic excitation, note that non-investigated discrepancies exist between the LXCat *Itikawa database* and the LXCat *Hayashi database*.

Table 7 Electronic excitation and ionization of atomic species by electron impact. The electron configuration and term are provided for each state. Rate coefficients are rounded in the present table and non-rounded values can be found in [90]**.**

Reaction		$k_f = A\ T_e^b \exp(-E/RT)$			Ref.
		A (cm^3s^{-1})	b	E/R (K)	
	Atomic electronic state transitions				
(R45)	$N(^4S^0) + e \leftrightarrow N(Y) + e$ $Y=^2D^0, ^2P^0, ^4P, ^2P, ^4P, ^2S^0, ^4D^0$	BOLSIG+			[88]
(R52)	$N(^2D^0) + e \leftrightarrow N(Y) + e$ $Y = ^2P^0, ^4P, ^2P, ^4P, ^2S^0, ^4D^0$	BOLSIG+			[88]
(R58)	$N(^2P^0) + e \leftrightarrow N(Y) + e$ $Y = ^4P, ^2P, ^4P, ^2S^0, ^4D^0$	BOLSIG+			[88]
(R63)	$N(^4P, 3s) + e \leftrightarrow N(Y) + e$ $Y = ^2P, ^4P, ^2S^0, ^4D^0$	BOLSIG+			[88]
(R67)	$N(^2P, 3s) + e \leftrightarrow N(Y) + e$ $Y = ^4P, ^2S^0, ^4D^0$	BOLSIG+			[88]
(R70)	$N(^4P, 2s^22p^4) + e \leftrightarrow N(Y) + e$ $Y = ^2S^0, ^4D^0$	BOLSIG+			[88]
(R72)	$N(^2S^0, 3p) + e \leftrightarrow N(^4D^0) + e$	BOLSIG+			[88]
(R73)	$O(^3P) + e \leftrightarrow O(^1D, ^1S) + e$	BOLSIG+			[89]
(R75)	$O(^1D) + e \leftrightarrow O(^1S) + e$	BOLSIG+			[89]
	Atomic electronic state ionization				
(R76)	$N(^4S^0) + e \leftrightarrow N^+ + 2e$	BOLSIG+			[88]
(R77)	$N(^2D^0) + e \leftrightarrow N^+ + 2e$	BOLSIG+			[88]
(R78)	$N(^2P^0) + e \leftrightarrow N^+ + 2e$	BOLSIG+			[88]
(R79)	$N(^4P, 3s) + e \leftrightarrow N^+ + 2e$	$9.33\ 10^{-10}$	0.49	49,120	[90]
(R80)	$N(^2P, 3s) + e \leftrightarrow N^+ + 2e$	$1.67\ 10^{-9}$	0.45	45,090	[90]
(R81)	$N(^4P, 2s^22p^4) + e \leftrightarrow N^+ + 2e$	$6.57\ 10^{-11}$	0.74	41,660	[90]
(R82)	$N(^2S^0, 3p) + e \leftrightarrow N^+ + 2e$	$3.74\ 10^{-9}$	0.42	34,580	[90]
(R83)	$N(^4D^0, 3p) + e \leftrightarrow N^+ + 2e$	$4.82\ 10^{-9}$	0.41	32,820	[90]
(R84)	$O(^3P) + e \leftrightarrow O^+ + 2e$	BOLSIG+			[89]
(R85)	$O(^1D) + e \leftrightarrow O^+ + 2e$	BOLSIG+			[89]
(R86)	$O(^1S) + e \leftrightarrow O^+ + 2e$	BOLSIG+			[89]

In the present work, we neglect[11] the formation of excited electronic states of N^+ and O^+. The forward rate coefficients of electron-impact ionization of the first three levels of N and O, (R76-R78) and (R84-86), are calculated with BOLSIG+ using the ionization cross-sections obtained by the B-spline R-matrix (BSR) approach [88,89]. For states above $N(^2D)$ and up to $N(^4D^0)$, the ionization rate coefficients calculated in [90] are used. We will show in Section 5 that the reactions listed in Table 7 drive the final stage of thermal spark ionization. A summary of the electronic levels of N_2, N, and O modeled in the present mechanism is given in Table 8.

[11] We also neglected the three-body recombination with heavy colliders, and therefore did not consider the following reaction, where A = N, O, and M is any heavy collider.

$$A + M \leftrightarrow A^+ + e + M$$

Table 8 Electronic levels of N_2, N, and O included in the present work. The energy is given relative to the ground state [105,106] **and *g* is the level statistical weight.**

State	Configuration	*g*	E_{up} (eV)
$N(^4S^0)$	$2s^22p^3$	4	0
$N(^2D^0)$	$2s^22p^3$	10	2.38
$N(^2P^0)$	$2s^22p^3$	6	3.575
$N(^4P)$	$2s^22p^2(^3P)3s$	12	10.33
$N(^2P)$	$2s^22p^2(^3P)3s$	6	10.68
$N(^4P)$	$2s^22p^4$	12	10.92
$N(^2S^0)$	$2s^22p^2(^3P)3p$	2	11.60
$N(^4D^0)$	$2s^22p^2(^3P)3p$	20	11.75
$O(^3P)$	$2s^22p^4$	9	0
$O(^1D)$	$2s^22p^4$	5	1.97
$O(^1S)$	$2s^22p^4$	1	4.19

State	*g*	E_{up} (eV)
$N_2(X\ ^1\Sigma_g^+)$	1	0
$N_2(A\ ^3\Sigma_u^+)$	3	6.23
$N_2(B\ ^3\Pi g)$	6	7.40
$N_2(a'\ ^1\Sigma_u^-)$	1	8.45
$N_2(C\ ^3\Pi_u)$	6	11.06
$N_2^+(X\ ^2\Sigma_g^+)$	2	0
$N_2^+(A\ ^2\Pi_u)$	4	1.13
$N_2^+(B\ ^2\Sigma_u^+)$	2	3.16
$N_2^+(C\ ^2\Sigma_u^+)$	2	8.02

Table 9 Supplementary reactions for the thermal spark transition. Quenching reactions are taken from [23] **and the ionization rate coefficients of N^+ and O^+ are calculated in this work.**

	Reaction & Temp. dependence		A ($cm^3\ s^{-1}$)	b	E/R (K)	Ref.
	Quenching of N_2 electronic excited states [23]					
(R87)	$N_2(A) + O_2 \leftrightarrow N_2(X) + 2O$	T_g	$9.81\ 10^{-14}$	0.5	0	[53]
(R88)	$N_2(A) + O_2 \leftrightarrow N_2(X) + O_2$	T_g	$4.33\ 10^{-14}$	0.5	0	[53]
(R89)	$N_2(A) + O \leftrightarrow NO + N(^2D)$	T_g	$4.00\ 10^{-11}$	0.0	0	[107]
(R90)	$N_2(B) + N_2 \leftrightarrow N_2(A) + N_2$	T_g	$1.00\ 10^{-11}$	0.0	0	[53]
(R91)	$N_2(B) + O_2 \leftrightarrow N_2(X) + 2O$	T_g	$3.00\ 10^{-10}$	0.0	0	[53]
(R92)	$N_2(B) + O \leftrightarrow NO + N(^2D)$	T_g	$3.00\ 10^{-10}$	0.0	0	[108]
(R93)	$N_2(C) + N_2 \leftrightarrow N_2(B) + N_2$	T_g	$1.00\ 10^{-11}$	0.0	0	[53]
(R94)	$N_2(C)+O_2 \leftrightarrow N_2(X)+O+O^*$	T_g	$1.73\ 10^{-11}$	0.3	0	[21]
(R95)	$N_2(C) + O \leftrightarrow NO + N(^2D)$	T_g	$3.00\ 10^{-10}$	0.0	0	[108]
(R96)	$N_2(a') + N_2 \leftrightarrow N_2(B) + N_2$	T_g	$2.00\ 10^{-13}$	0.0	0	[109]
(R97)	$N_2(a')+O_2 \leftrightarrow N_2(X)+O+O^*$	T_g	$2.80\ 10^{-11}$	0.0	0	[109]
(R98)	$N_2(a') + O \leftrightarrow NO + N(^2D)$	T_g	$3.00\ 10^{-10}$	0.0	0	[108]
	Formation of doubly ionized ions					
(R99)	$N^+ + e \leftrightarrow N^{++} + 2e$	T_e	$5.10\ 10^{-12}$	0.68	349,690	This work
(R100)	$O^+ + e \leftrightarrow O^{++} + 2e$	T_e	$9.42\ 10^{-14}$	0.98	381,240	This work

The quenching of N_2 excited states is mainly taken from the work of Popov [23], which is, to our knowledge, the most complete set of reactions for the simulation of non-thermal nanosecond discharges. It was shown in [23] that this set reproduces the ultrafast heating observed in [21] and [16,110] with good accuracy. The quenching rate coefficients of $N_2(A)$ given in Table 9 are slightly modified compared to those of Popov because our model is not vibrational specific and does not include O_2 excited states. Therefore, it was assumed in (R88) that O_2 is not excited to the $O_2(b^1\Sigma_g^+)$ state, which is different from the *(R2)* reaction in [23].

Also, we discarded the *(R3)*, *(R4)* and *(R6)* reactions of [23] because they involve vibrationally excited molecules. The formation of NO by $N_2(A)$ quenching, (R92), was neglected in the early work of Popov [111]. However, it was

shown in [107] and later in [108,112] that the formation of NO may have a higher impact than originally expected, which motivates its addition to this mechanism.

For the conditions of Rusterholtz *et al.* [21], Popov showed that the dissociative quenching of N_2(A, B, C, a') represent 63% of the total oxygen dissociation [21,23]. Regarding the production of metastable oxygen by N_2(C) quenching, Popov used the branching ratio (46% / 52% / 2%) of metastable argon quenching by O_2 [22,113]. The quenching of metastable xenon, which has a similar energy as N_2(B), does not produce excited atomic oxygen [113]. Therefore, we assume that only $O(^3P)$ is produced in N_2(B) quenching. Note that Popov used a rate coefficient constant with temperature for N_2(C) quenching, although it was shown that the rate varies with $T_g^{0.3}$ [21]. The product of N_2(a') quenching is assumed to be $O(^3P) + O(^1D)$ with a probability of one [23]. We neglect as well the quenching of $N(^2D)$ and $O(^1S, ^1D)$, reactions *(R16)* to *(R34)* in [23], because these reactions induce vibrational excitation, which is not included in the present mechanism. The quenching of $N(^2P)$ by N_2 was also neglected [114]. Using the rates from [50,53,54], we found that the formation and recombination of N_3^+ induce negligible variations to the formation of the thermal spark. Therefore, the N_3^+ chemistry is not included in this work.

Finally, the formation of N^{++} and O^{++} by electron-impact of N^+ and O^+ is included, (R99) and (R100). We integrated the cross-sections reported in [115] with a Maxwellian EEDF and fitted the results with Arrhenius laws. These Arrhenius rate coefficients fit the integrated results within 1% in the 40,000 – 73,000 K range, see Table 10, which corresponds to the range of temperature where these reactions have a significant impact.

Table 10 Deviation of the Arrhenius fits compared to rates calculated from the cross-sections of N^+ and O^+ ionization by electron impact, (R99) and (R100).

	23,000 K	30,000 K	40,000 K	73,000 K
$N^+ \rightarrow N^{++}$	~ 1%	< 1%	< 1%	< 1%
$O^+ \rightarrow O^{++}$	~ 30%	~ 10%	~ 1%	< 1%

Note that this set of reactions is incomplete if one is interested in the heating generated by *non-thermal* sparks. For that purpose, the quenching of atomic metastable states may have to be included [49] along with other species such as O^-, O_3, N_3^+, and N_4^+ [50].

5. Comparison of the numerical kinetics with the experimental findings

As briefly mentioned before, we previously performed the simulation of canonical discharges in air to explain the formation of a fully ionized plasma in less than 10 ns [26]. In the present study, using a lighter baseline mechanism allows for the inclusion of the reverse rates of the reactions presented in Section 4.c. The chemical mechanism also gained clarity. Another novelty compared to [26] is the inclusion of N^{++} and O^{++} formation. Moreover, in the present work, an experimental voltage waveform is employed to calculate the reduced electric field. The applied voltage is calculated by summing the incident and reflected waveforms. We will show in this section that the sub-nanosecond transition to a fully ionized plasma is still driven by the formation of the excited electronic states of N and O, noted N* and O* here, and follows the same path as extensively described in [26]. The simulation is computationally expensive when accounting for electron-electron collisions in the EEDF calculation. The reader interested in conducting these simulations at a reduced CPU cost could assume a Boltzmann EEDF for an ionization fraction above 1%, which provides very similar results – see Figure 11 of [26].

Table 11 Initial conditions and numerical parameters. The initial N_2 and O_2 number densities correspond to air at 0.1 MPa (1 atm) and 300 K, and the initial electron and N_2^+ number densities to typical ionization in streamer discharges.

Initial gas state	Numerical parameters

N_2 (cm^{-3})	O_2 (cm^{-3})	N_2^+ (cm^{-3})	e- (cm^{-3})	T_{gas} (K)	T_e (K)	Time step (ps)
1.90×10^{19}	5.06×10^{18}	10^{14}	10^{14}	300	1000	1.0

a. Comparison to electrical measurements

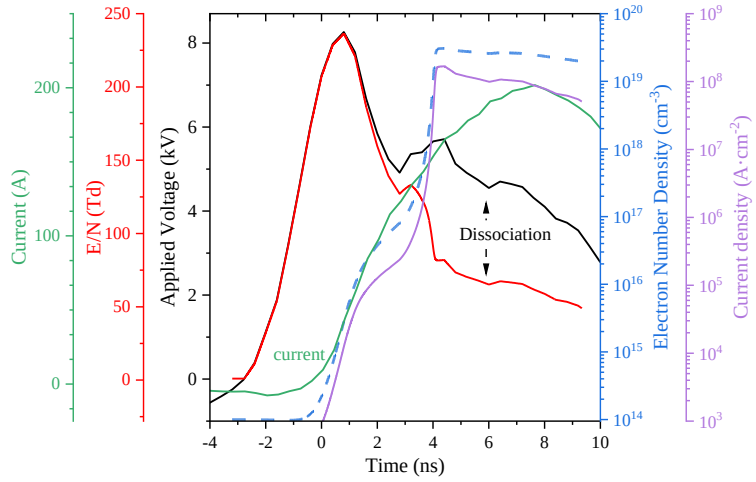

Figure 9 *Experimental:* Applied voltage (black) and current (green), both reconstructed from the difference between the incident and reflected pulses. *Numerical:* reduced field (red line), current density (purple), and electron number density (in blue).

The simulation uses the initial conditions and numerical parameters listed in Table 11. The time t = 0 ns is arbitrarily defined as the first measurement of the electron number density by Stark broadening of H_α with enough signal-to-noise ratio. This instant corresponds approximately to the top of the voltage ramp and the rise of the current. The applied voltage on the 1.2-mm gap is represented in Figure 9 and was reconstructed from the anode and cathode voltage pulse shapes. The reduced field, E/N, is calculated in the simulation at each time step, assuming a Laplacian field between the electrodes and accounting for the density change due to N_2 and O_2 dissociation. The reduced field is arbitrarily reduced by 10% to account for the cathode fall (900 V at maximal applied voltage). In BOLSIG+, the reduced field E/N is usually defined as the ratio of the electric field to the neutral particle density, $N_{neutral}$. However, the neutral particle number density can drop to negligible values. Thus, the reduced field tends toward infinity and the electron temperature increases above reasonable values. Therefore, we define N as the heavy particle density, *i.e.* $N = N_{ion} + N_{neutral}$ [26,86]. This assumption, initially proposed in [26,86], was also successfully employed in [116].

In Figure 9, the experimental current going through the discharge gap has been reconstructed by synchronizing and summing the incident and reflected current pulses. For t < 4 ns, the typical diameter of the partially ionized plasma is 200 – 300 µm [25], which corresponds to current densities of $j = 10^4 – 10^5$ A·cm^{-2} typically found in non-thermal sparks [21,23]. Similar values are found in the simulation up to t = 4 ns. Near t = 4 – 8 ns, the optical diameter measured with the ionic lines is ~1 µm (Figure 6) and the measured current reaches 150 – 200 A, which corresponds to $j \sim 5\cdot10^9$ A·cm^{-2} when the simulation predicts a lower value (10^8 A·cm^{-2}). Several phenomena could explain this difference:

1. The current density measurement is rather sensitive to the discharge diameter measurement, because $j \propto 1/d^2$, and this difference could be reduced if the diameter were a few µm larger.
2. As observed in [36], there could be a multi-filament structure partially out of the spectrometer field of view.

3. Finally, parallel to the fully ionized core (~ 1 µm), a portion of the current might flow through an outer shell of the plasma channel (~ 100 µm) and have a non-negligible contribution. For instance, assuming the current flowing through the outer shell is the same after the filament formation (i.e. I_{out} ~ 100 A) would reduce the experimental current density in the core down to $j \sim 2 \cdot 10^9$ A·cm^{-2}.

Finally, for t ~ 10 ns, the current is still ~100 A but the diameter increases to 10 µm, which decreases the measured current density down to $j \sim 10^7 - 10^8$ A·cm^{-2}, close to what the simulation indicates.

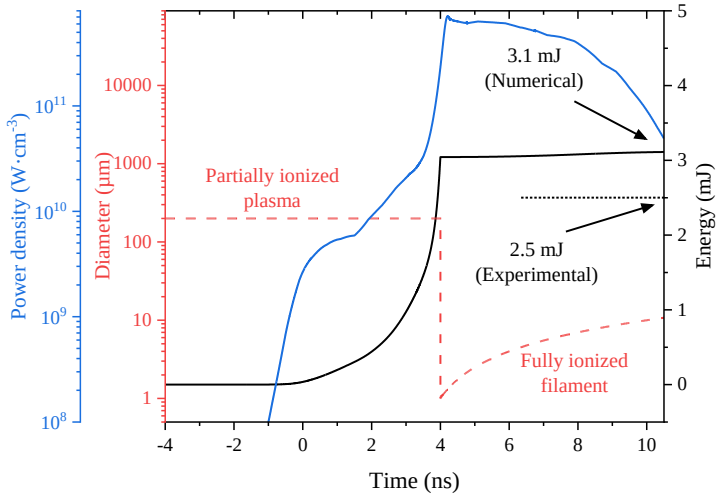

Figure 10 Simplified discharge diameter evolution (red) used to compute the deposited energy (black) in the 0-D approximation from the simulated power (blue). The numerical value of the deposited energy (3.7 mJ) is close to the experimental one (2.5 mJ).

From our measurements in Section 3.b, a simplified evolution of the discharge diameter is used to calculate the deposited power, see Figure 10. The discharge power, P [W], is calculated from the power density, $E \times j$ [W·cm^{-3}], multiplied by the discharge volume. The deposited energy, shown in Figure 10 from the time integration of P, starts increasing from t = 0 ns, which corresponds to our first measurement of the electron number density by Stark broadening. From 0 ns to 4 ns, the discharge diameter is assumed to be constant (d = 200 µm), as documented in our previous work [25]. The deposited energy sharply increases up to ~ 3.6 mJ, close to the experimental value of 2.5 mJ. From this time step, the discharge diameter drops, as shown by sub-nanosecond imaging in [25], down to d = 1 µm. For t > 4 ns, the diameter is assumed to increase linearly, see Section 3.b. This small diameter compensates for a high power density of 10^{11} W·cm^{-3} and the deposited energy slowly varies for t > 4 ns. The presence of an outer shell of a partially ionized plasma ($n_e \sim 10^{16}$-10^{17} cm^{-3} and $j = 10^5$ A·cm^2) would only slightly increase the total deposited energy by a few mJ.

Based on the current and energy comparison performed in this subsection, we consider the 0-D formalism sufficient to reproduce the main trends of the thermal spark formation. In the following subsection, the channels of electron formation are identified and compared to the experimental trends.

b. Comparison to optical measurements

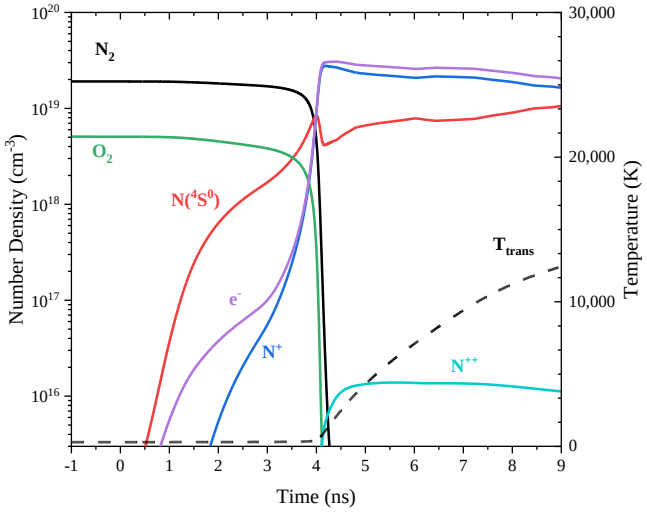

Figure 11 Evolution of the species number densities and temperature during the thermal spark transition in air. Atomic O and O^+ are omitted for clarity, but they follow the same trends as N and N^+.

In this section, we compare the optical measurements near the cathode and the simulation. The evolution of the plasma composition is shown in Figure 11 and follows the same behavior as the one reported in our previous work [26]. It is convenient to describe the number density evolution with, in Figure 12, the normalized electron number density variations, ν_e [s^{-1}], and the ionization frequency, $\nu_{ion,k}$ [s^{-1}], of reaction k where $Q_{ion,k}$ [$cm^{-3}{\cdot}s^{-1}$] is the electron production rate of reaction k and $Q_{rev,k}$ [$cm^{-3}{\cdot}s^{-1}$] the recombination rate in the reverse direction:

$$\nu_e = \frac{1}{n_e}\frac{dn_e}{dt} \qquad \text{Eq. 16}$$

$$\nu_{ion,k} = \frac{Q_{ion,k} - Q_{rev,k}}{n_e} \qquad \text{Eq. 17}$$

For t < 1 ns and according to the data in Figure 11 and Figure 12, the plasma remains partially ionized and is mostly composed of N_2 and O_2. At t = 1 ns, atomic nitrogen is quickly formed via the dissociation of electronic states of N_2 [26,42]. Ionization is driven by electron-impact on N_2 and O_2, while the ionization of N_2 excited electronic states gets stronger than that of O_2. The ionization fraction reaches ~1% and ~10% of N_2 is dissociated into N. The ionization frequencies by electron impact on $N_2(X)$ and N_2^* are approximately equal but, for t > 1 ns, are both decreasing with time due to molecular dissociation, see Figure 12 (left). This fall of the ionization frequency from N_2 and N_2^* for t > 1ns is compensated by an increase of the ionization frequency of N. The dissociative recombination of NO^+, N_2^+, and O_2^+ induces a non-negligible drop in the total ionization frequency remaining near 1 GHz. The ionization frequency by N, $\nu_{ion,N}$, is first dominated by $N(^2D^0)$, see Figure 12 (right). From t > 1 ns, the ionization frequencies from states above $N(^2D^0)$ start dominating the ionization process. In practice, the addition of states higher than $N(^4P)$ at 10.92 eV does not significantly alter the kinetics of electron formation (comparison not shown). Near t = 3 ns, the dissociative recombination of molecules is negligible, and the reverse rate of N and O ionization is the dominant recombination channel. At this instant and in an interval of Δt = 0.5 ns, n_e gains almost three orders of magnitude. Consequently, the ion-electron thermalization time, inversely proportional to n_e, significantly decreases below the nanosecond scale [1,26]. This sharp increase of n_e drives the translational temperature thermalization with T_e via electron-ion collisions, see also Figure 8 of [26]. The translational temperature, in Figure 11, reaches values near 10,000 K, below the

~30,000 K simulated in our previous work [26] and Shcherbanev et al. [42] because E/N quickly drops below 50 Td. Note that if these simulations included the magnetic compression effect, the translational temperature would be higher, but the inclusion of this effect falls outside of the presented 0-D formalism. After t = 4 ns, the plasma is fully ionized and composed mainly of electrons, N^+ and O^+.

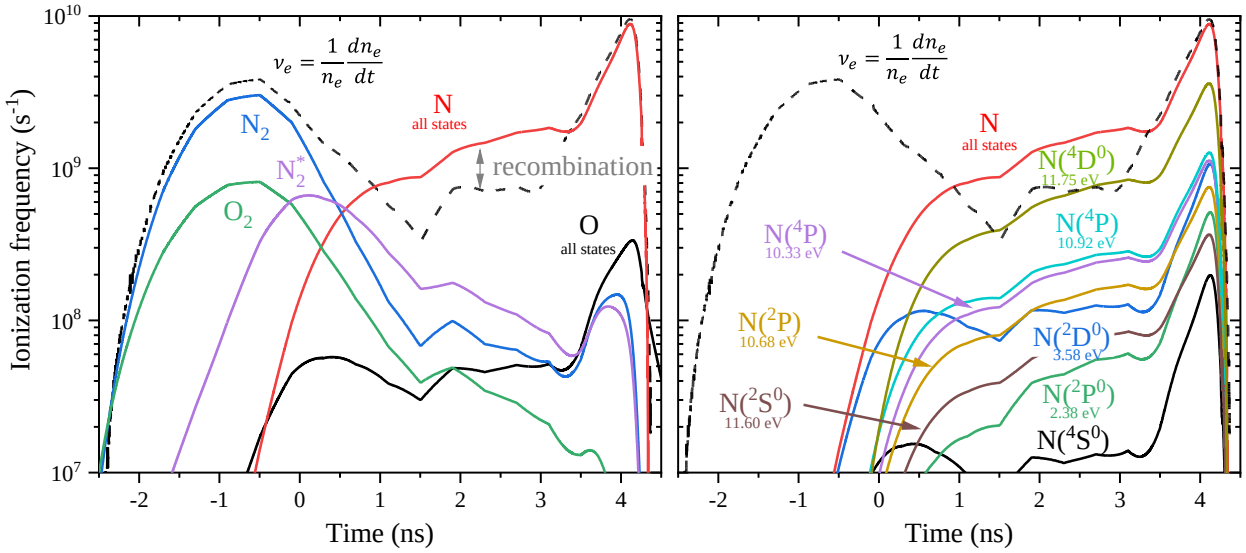

Figure 12 Evolution of the effective ionization frequency, ν_e in dashed black, compared to the ionization frequency through the channels of ionization, $\nu_{ion,k}$ in full lines. (left) Sum of the ionization channels by electron impact of N_2, O_2, O and N. Only the major channels are shown and the recombination channels are hidden for clarity. (right) Detailed contributions of each electronic state of N.

The sharp increase of the ionization frequency at t = 3.5 ns is also influenced by the following mechanism. The increase of n_e induces a faster ionization rate (by electron impact) and a faster formation of N* and O* (by electron impact). The ionization cross-sections of these electronic states present higher amplitudes and lower ionization thresholds than those of the electronic ground state. In parallel, the increase of n_e shifts the underpopulated high-energy tail of the EEDF closer to a Boltzmann distribution, see for instance Figure 9 of [26]. Therefore, the ionization rate is significantly increased. All these retroactive loops lead to a dramatic increase in the electron number density.

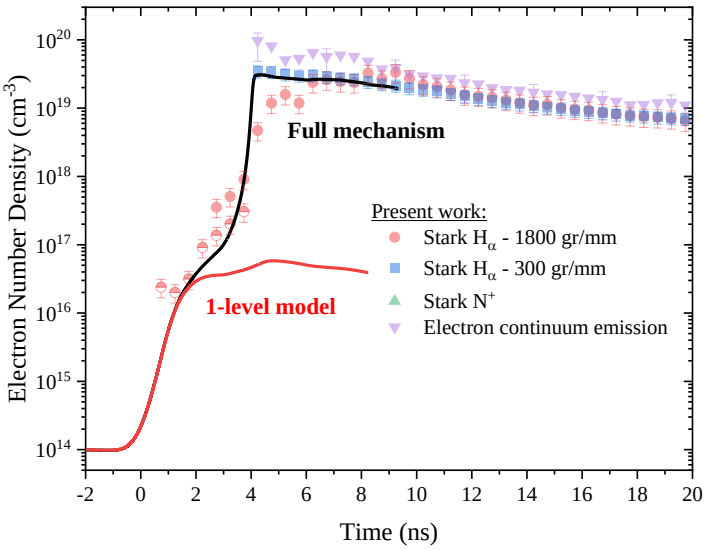

Figure 13 Comparison of the electron number density obtained by simulation (black solid line) with measurements performed by Stark broadening and continuum emission. Full ionization is not reached if the simulation is run without the ionization of O and N excited states (red solid line).

Figure 13 compares the evolution of the electron number density measured with Stark broadening of N^+, Stark broadening of H_α, and the free-free/free-bound continuum, with the electron number density calculated with our kinetic mechanism. The "1-level model" corresponds to the mechanism of Section 4.c with all reactions except the formation and ionization of N* and O*. In this case, n_e reaches at most $3 \cdot 10^{16}$ cm^{-3} at the end of the 10-ns pulse. With the "Full mechanism", the electron-impact ionization of the first eight electronic states of N and three electronic states of O is added. The very abrupt ionization phase matches the one observed in the experiments. Note that the two simulations agree for $t < 1$ ns as expected when, below an ionization fraction of 1%, the kinetics of atomic excited electronic states is not primarily driving the chemistry.

The decay of n_e at later times is due to an isentropic expansion lasting more than 100 ns [25,28]. In these simulations, it was assumed that the discharge volume is constant, which is usually correct in non-thermal nanosecond discharges. We believe that the agreement would be improved if the model included the plasma channel expansion, which could begin as early as $t = 6$ ns, see also Figure 6. The consideration of the radiative losses, which could be non-negligible but not dominant (see [25,26]), would also represent an improvement [117]. Although this 0-D approximation is suitable for capturing the main trends of the thermal spark formation, a 1-D formalism would also be helpful to quantitatively assess the second-order influence of the magnetic compression.

6. Conclusions

In this work, we study the formation of thermal sparks generated at ambient conditions by an 8-kV pulse of 10 ns across a 1.2-mm gap. In the first part, the increase of the electron number density near the cathode is measured using several optical emission spectroscopy methods. First, the Stark broadening of H_α, at 656 nm, and N^+, at 500 nm, are used. Then, after intensity calibration of the emission spectrum near $\lambda = 500$ nm, the optical diameter of the discharge is obtained with sub-nanosecond resolution from atomic ion lines by assuming plasma neutrality. This diameter indicates that magnetic compression is likely to play a role during a few nanoseconds and is later used to determine the electron number density via the continuum radiation near $\lambda = 500$ nm. The three methods used to measure n_e agree with one another and show that the thermal spark's full ionization occurs on a timescale of approximately 0.5 ns.

In the second part of this article, a 0-D kinetic mechanism is developed to explain the observed abrupt increase of the ionization degree of the nanosecond thermal spark. The mechanism includes N_2, O_2, NO, N, O, N_2^+, O_2^+, NO^+, N^+, O^+, N^{++}, and O^{++} species. The novelty of the present kinetic mechanism is the addition of the ionization of the excited electronic states of N and O by electron impact. These reactions are found to be essential to reproduce the experimental data obtained in the first part of the article. The agreement between simulations and experiments strongly supports the key role of the atomic excited states in the ionization of the thermal spark filaments. However, the topology and the propagation of the fully ionized filaments remain unclear and require further investigation. Including the electron-impact ionization of N and O excited states in 1-D or 2-D simulations, together with incorporating plasma-electrode interactions, runaway electrons, magnetic compression, radiation, and ionization wave propagation would help to further describe the nanosecond thermal spark.

7. Acknowledgments

This work has been supported by the French National Research Agency (ANR-16-CE22-0005 PASTEC, ANR-16-CE30-0004 ASPEN). Dr Nicolas Minesi has been supported by an IDEX Ph.D. fellowship (ANR-11-IDEX-0003-02). The authors express their gratitude to all the contributors of LXCat, BOLSIG+, and ZDPlasKin. We thank the anonymous reviewers for their valuable comments and feedback.

8. References

[1] Raizer, Y. P. *Gas Discharge Physics*. Springer Verlag. Berlin., 1991.

[2] Maly, R., and Vogel, M. “Initiation and Propagation of Flame Fronts in Lean CH4-Air Mixtures by the Three Modes of the Ignition Spark.” *Symposium (International) on Combustion*, Vol. 17, 1979, pp. 821–831. https://doi.org/10.1016/S0082-0784(79)80079-X.

[3] Nagulapally, M., Candler, G., Laux, C., Yu, L., Packan, D., Kruger, C., Stark, R., and Schoenbach, K. “Experiments and Simulations of DC and Pulsed Discharges in Air Plasmas.” *31st AIAA Plasmadynamics and Lasers Conference*, 2000, p. AIAA paper 2000-2417. https://doi.org/10.2514/6.2000-2417.

[4] Adamovich, I., Baalrud, S. D., Bogaerts, A., Bruggeman, P. J., Cappelli, M., Colombo, V., Czarnetzki, U., Ebert, U., Eden, J. G., Favia, P., Graves, D. B., Hamaguchi, S., Hieftje, G., Hori, M., Kaganovich, I. D., Kortshagen, U., Kushner, M. J., Mason, N. J., Mazouffre, S., Thagard, S. M., Metelmann, H. R., Mizuno, A., Moreau, E., Murphy, A. B., Niemira, B. A., Oehrlein, G. S., Petrovic, Z. L., Pitchford, L. C., Pu, Y. K., Rauf, S., Sakai, O., Samukawa, S., Starikovskaia, S., Tennyson, J., Terashima, K., Turner, M. M., Van De Sanden, M. C. M., and Vardelle, A. The 2017 Plasma Roadmap: Low Temperature Plasma Science and Technology. *Journal of Physics D: Applied Physics*. 32. Volume 50, 323001. https://doi.org/10.1088/1361-6463/aa76f5.

[5] Vincent-Randonnier, A. Combustion Enhancement and Stabilization: Principles of Plasma Assistance and Diagnostics Tools. In *Handbook of Combustion*, Wiley-VCH Verlag GmbH & Co. KGaA, Weinheim, Germany, 2010.

[6] Starikovskaia, S. M. “Plasma-Assisted Ignition and Combustion: Nanosecond Discharges and Development of Kinetic Mechanisms.” *Journal of Physics D: Applied Physics*, Vol. 47, No. 35, 2014, p. 353001. https://doi.org/10.1088/0022-3727/47/35/353001.

[7] Fridman, G., Friedman, G., Gutsol, A., Shekhter, A. B., Vasilets, V. N., and Fridman, A. “Applied Plasma Medicine.” *Plasma Processes and Polymers*, Vol. 5, No. 6, 2008, pp. 503–533. https://doi.org/10.1002/ppap.200700154.

[8] Laux, C., Yu, L., Packan, D. M., Gessman, R. J., Pierrot, L., Kruger, C. H., and Zare, R. “Ionization Mechanisms in Two-Temperature Air Plasmas.” *30th Plasmadynamic and Lasers Conference*, 1999, p. AIAA paper 99-3476. https://doi.org/10.2514/6.1999-3476.

[9] Pai, D. Z., Lacoste, D. A., and Laux, C. O. “Transitions between Corona, Glow, and Spark Regimes of Nanosecond Repetitively Pulsed Discharges in Air at Atmospheric Pressure.” *Journal of Applied Physics*, Vol. 107, No. 9, 2010, p. 093303. https://doi.org/10.1063/1.3309758.

[10] Pai, D. Z., Stancu, G. D., Lacoste, D. A., and Laux, C. O. “Nanosecond Repetitively Pulsed Discharges in Air at Atmospheric Pressure - The Glow Regime.” *Plasma Sources Science and Technology*, Vol. 18, No. 4, 2009, p. 045030. https://doi.org/10.1088/0963-0252/18/4/045030.

[11] Pai, D. Z., Lacoste, D. A., and Laux, C. O. “Nanosecond Repetitively Pulsed Discharges in Air at Atmospheric Pressure-the Spark Regime.” *Plasma Sources Science and Technology*, Vol. 19, No. 6, 2010, p. 065015. https://doi.org/10.1088/0963-0252/19/6/065015.

[12] Colonna, G., Laporta, V., Celiberto, R., Capitelli, M., and Tennyson, J. “Non-Equilibrium Vibrational and Electron Energy Distributions Functions in Atmospheric Nitrogen Ns Pulsed Discharges and Ms Post-Discharges: The Role of Electron Molecule Vibrational Excitation Scaling-Laws.” *Plasma Sources Science and Technology*, Vol. 24, No. 3, 2015, p. 35004. https://doi.org/10.1088/0963-0252/24/3/035004.

[13] Pietanza, L. D., Colonna, G., D’Ammando, G., Laricchiuta, A., and Capitelli, M. “Vibrational Excitation and Dissociation Mechanisms of CO2 under Non-Equilibrium Discharge and Post-Discharge Conditions.” *Plasma Sources Science and Technology*, Vol. 24, No. 4, 2015, p. 42002. https://doi.org/10.1088/0963-0252/24/4/042002.

[14] Verreycken, T., van Gessel, A. F. H., Pageau, A., and Bruggeman, P. “Validation of Gas Temperature Measurements by OES in an Atmospheric Air Glow Discharge with Water Electrode Using Rayleigh Scattering.” *Plasma Sources Science and Technology*, Vol. 20, No. 2, 2011, p. 024002. https://doi.org/10.1088/0963-0252/20/2/024002.

[15] Simeni, M. S., Zheng, Y., Barnat, E. V, and Bruggeman, P. J. “Townsend to Glow Discharge Transition for a Nanosecond Pulse Plasma in Helium: Space Charge Formation and Resulting Electric Field Dynamics.” *Plasma Sources Science and Technology*, Vol. 30, No. 5, 2021, p. 055004. https://doi.org/10.1088/1361-6595/abf320.

[16] Lo, A., Cessou, A., Boubert, P., and Vervisch, P. “Space and Time Analysis of the Nanosecond Scale Discharges in Atmospheric Pressure Air: I. Gas Temperature and Vibrational Distribution Function of N_2 and O_2.” *Journal of Physics D: Applied Physics*, Vol. 47, No. 11, 2014, p. 115201. https://doi.org/10.1088/0022-3727/47/11/115201.

[17] Dawson, R., and Little, J. “Characterization of Nanosecond Pulse Driven Dielectric Barrier Discharge Plasma Actuators for Aerodynamic Flow Control.” *Journal of Applied Physics*, Vol. 113, No. 10, 2013, p. 103302. https://doi.org/10.1063/1.4794507.

[18] Jans, E. R., Raskar, S., Yang, X., and Adamovich, I. V. “Kinetics of Metastable N2(A3Σu+, v) Molecules in High-Pressure Nonequilibrium Plasmas.” *Plasma Sources Science and Technology*, Vol. 30, No. 2, 2021, p. 025003. https://doi.org/10.1088/1361-6595/abcc7c.

[19] Shcherbanev, S. A., Stepanyan, S. A., Popov, N. A., and Starikovskaia, S. M. “Dielectric Barrier Discharge for Multi-Point Plasma-Assisted Ignition at High Pressures.” *Philosophical Transactions of the Royal Society A: Mathematical, Physical and Engineering Sciences*, Vol. 373, No. 2048, 2015, p. 20140342. https://doi.org/10.1098/rsta.2014.0342.

[20] Stepanyan, S., Minesi, N., Tibère-Inglesse, A., Salmon, A., Stancu, G. D., and Laux, C. O. “Spatial Evolution of the Plasma Kernel Produced by Nanosecond Discharges in Air.” *Journal of Physics D: Applied Physics*, Vol. 52, No. 29, 2019, p. 295203. https://doi.org/10.1088/1361-6463/ab1ba4.

[21] Rusterholtz, D. L., Lacoste, D. A., Stancu, G. D., Pai, D. Z., and Laux, C. O. “Ultrafast Heating and Oxygen Dissociation in Atmospheric Pressure Air by Nanosecond Repetitively Pulsed Discharges.” *Journal of Physics D: Applied Physics*, Vol. 46, No. 46, 2013, p. 464010. https://doi.org/10.1088/0022-3727/46/46/464010.

[22] Popov, N. A. “Fast Gas Heating in a Nitrogen–Oxygen Discharge Plasma: I. Kinetic Mechanism.” *Journal of Physics D: Applied Physics*, Vol. 44, No. 28, 2011, p. 285201. https://doi.org/10.1088/0022-

3727/44/28/285201.

[23] Popov, N. A. “Pulsed Nanosecond Discharge in Air at High Specific Deposited Energy: Fast Gas Heating and Active Particle Production.” *Plasma Sources Science and Technology*, Vol. 25, No. 4, 2016, p. 44003. https://doi.org/10.1088/0963-0252/25/4/044003.

[24] Pai, D. Z. *Nanosecond Repetitively Pulsed Plasmas in Preheated Air at Atmospheric Pressure*. Ecole Centrale Paris, PhD Thesis, 2008.

[25] Minesi, N., Stepanyan, S., Mariotto, P., Stancu, G. D., and Laux, C. O. “Fully Ionized Nanosecond Discharges in Air: The Thermal Spark.” *Plasma Sources Science and Technology*, Vol. 29, 2020, p. 85003. https://doi.org/10.1088/1361-6595/ab94d3.

[26] Minesi, N., Mariotto, P., Pannier, E., Stancu, G. D., and Laux, C. O. “The Role of Excited Electronic States in Ambient Air Ionization by a Nanosecond Discharge.” *Plasma Sources Science and Technology*, Vol. 30, No. 3, 2021, p. 035008. https://doi.org/10.1088/1361-6595/abe0a3.

[27] Minesi, N. Q., Blanchard, V. P., Pannier, E., Stancu, G. D., and Laux, C. O. “Plasma-Assisted Combustion with Nanosecond Discharges. I: Discharge Effects Characterization in the Burnt Gases of a Lean Flame.” *Plasma Sources Science and Technology*, Vol. 31, No. 4, 2022, p. 045029. https://doi.org/10.1088/1361-6595/ac5cd4.

[28] Lo, A., Cessou, A., Lacour, C., Lecordier, B., Boubert, P., Xu, D. A., Laux, C. O., and Vervisch, P. “Streamer-to-Spark Transition Initiated by a Nanosecond Overvoltage Pulsed Discharge in Air.” *Plasma Sources Science and Technology*, Vol. 26, No. 4, 2017, p. 45012. https://doi.org/10.1088/1361-6595/aa5c78.

[29] Sainct, F. *Etude de La Réactivité de Décharges Électriques Nanoseconde à La Pression Atmosphérique Dans La Vapeur d’eau*. https://hal.archives-ouvertes.fr/tel-01020267, Ecole Centrale Paris, PhD Thesis, in French, 2014.

[30] Sainct, F. P., Urabe, K., Pannier, E., Lacoste, D. A., and Laux, C. O. “Electron Number Density Measurements in Nanosecond Repetitively Pulsed Discharges in Water Vapor at Atmospheric Pressure.” *Plasma Sources Science and Technology*, Vol. 29, 2020, p. 025017. https://doi.org/10.1088/1361-6595/ab681b.

[31] van der Horst, R. M., Verreycken, T., van Veldhuizen, E. M., and Bruggeman, P. J. “Time-Resolved Optical Emission Spectroscopy of Nanosecond Pulsed Discharges in Atmospheric-Pressure N 2 and N 2 /H 2 O Mixtures.” *Journal of Physics D: Applied Physics*, Vol. 45, No. 34, 2012, p. 345201. https://doi.org/10.1088/0022-3727/45/34/345201.

[32] Orriere, T., Moreau, E., and Pai, D. Z. “Ionization and Recombination in Nanosecond Repetitively Pulsed Microplasmas in Air at Atmospheric Pressure.” *Journal of Physics D: Applied Physics*, Vol. 51, No. 49, 2018, p. 494002. https://doi.org/10.1088/1361-6463/aae134.

[33] Shao, T., Zhang, C., Niu, Z., Yan, P., Tarasenko, V. F., Baksht, E. K., Kostyrya, I. D., and Shutko, V. “Runaway Electron Preionized Diffuse Discharges in Atmospheric Pressure Air with a Point-to-Plane Gap in Repetitive Pulsed Mode.” *Journal of Applied Physics*, Vol. 109, No. 08, 2011, p. 083306. https://doi.org/10.1063/1.3581066.

[34] Shao, T., Tarasenko, V. F., Zhang, C., Lomaev, M. I., Sorokin, D. A., Yan, P., Kozyrev, A. V., and Baksht, E. K. “Spark Discharge Formation in an Inhomogeneous Electric Field under Conditions of Runaway Electron Generation.” *Journal of Applied Physics*, Vol. 111, No. 2, 2012, p. 023304. https://doi.org/10.1063/1.3677951.

[35] Parkevich, E. V., Khirianova, A. I., Agavonov, A. V., Tkachenko, S. I., Mingaleev, A. R., Shelkovenko, T. A., Oginov, A. V., and Pikuz, S. A. “Anode Plasma Formation at the Initial Stage of a Nanosecond Air Discharge.” *Journal of Experimental and Theoretical Physics*, Vol. 126, No. 3, 2018, pp. 422–429. https://doi.org/10.1134/S1063776118030160.

[36] Parkevich, E. V., Medvedev, M. A., Ivanenkov, G. V., Khirianova, A. I., Selyukov, A. S., Agafonov, A. V., Korneev, P. A., Gus’Kov, S. Y., and Mingaleev, A. R. “Fast Fine-Scale Spark Filamentation and Its Effect on the Spark Resistance.” *Plasma Sources Science and Technology*, Vol. 28, No. 09, 2019, p. 095003.

https://doi.org/10.1088/1361-6595/ab3768.

[37] Parkevich, E. V., Medvedev, M. A., Agafonov, A. V, Tkachenko, S. I., Oginov, A. V, Khirianova, A. I., Mingaleev, A. R., Shelkovenko, T. A., and Pikuz, S. A. "The Peculiarities of Near-Cathode Processes in Air Discharge at Atmospheric Pressure." 2018, p. 1804.01336.

[38] Khirianova, A., Parkevich, E., Medvedev, M., Smaznova, K., Khirianov, T., Varaksina, E., and Selyukov, A. "Extraction of High-Contrast Diffraction Patterns of Fine-Structured Electrical Sparks from Laser Shadowgrams." *Optics Express*, Vol. 29, No. 10, 2021, p. 14941. https://doi.org/10.1364/oe.421460.

[39] Stritzke, P., Sander, I., and Raether, H. "Spatial and Temporal Spectroscopy of a Streamer Discharge in Nitrogen." *Journal of Physics D: Applied Physics*, Vol. 10, No. 16, 1977, pp. 2285–2300. https://doi.org/10.1088/0022-3727/10/16/019.

[40] Albrecht, H., Bloss, W. H., Herden, W. H., Maly, R., Saggau, B., and Wagner, E. "New Aspects on Spark Ignition." *SAE Technical Papers*, 1977, p. 770853. https://doi.org/10.4271/770853.

[41] Houpt, A. W., and Leonov, S. B. "Charge Transfer in Constricted Form of Surface Barrier Discharge at Atmospheric Pressure." *Journal of Thermophysics and Heat Transfer*, Vol. 31, 2016, pp. 1–9. https://doi.org/10.2514/1.T4970.

[42] Shcherbanev, S. A., Ding, C., Starikovskaia, S. M., and Popov, N. A. "Filamentary Nanosecond Surface Dielectric Barrier Discharge. Plasma Properties in the Filaments." *Plasma Sources Science and Technology*, Vol. 28, No. 6, 2019, p. 065013. https://doi.org/10.1088/1361-6595/ab2230.

[43] Shcherbanev, S. A., Yu Khomenko, A., Stepanyan, S. A., Popov, N. A., and Starikovskaia, S. M. "Optical Emission Spectrum of Filamentary Nanosecond Surface Dielectric Barrier Discharge." *Plasma Sources Science and Technology*, Vol. 26, No. 2, 2016, p. 02LT01. https://doi.org/10.1088/1361-6595/26/2/02LT01.

[44] Stepanyan, S. A., Starikovskiy, A. Y., Popov, N. A., and Starikovskaia, S. M. "A Nanosecond Surface Dielectric Barrier Discharge in Air at High Pressures and Different Polarities of Applied Pulses: Transition to Filamentary Mode." *Plasma Sources Science and Technology*, Vol. 23, No. 4, 2014, p. 045003. https://doi.org/10.1088/0963-0252/23/4/045003.

[45] Ding, C., Jean, A., Popov, N. A., and Starikovskaia, S. M. "Fine Structure of Streamer-to-Filament Transition in High-Pressure Nanosecond Surface Dielectric Barrier Discharge." *Plasma Sources Science and Technology*, Vol. 31, No. 4, 2022, p. 045013. https://doi.org/10.1088/1361-6595/ac5c5f.

[46] Parkevich, E. V., Medvedev, M. A., Khirianova, A. I., Ivanenkov, G. V., Selyukov, A. S., Agafonov, A. V., Shpakov, K. V., and Oginov, A. V. "Extremely Fast Formation of Anode Spots in an Atmospheric Discharge Points to a Fundamental Ultrafast Breakdown Mechanism." *Plasma Sources Science and Technology*, Vol. 28, No. 12, 2019, p. 125007. https://doi.org/10.1088/1361-6595/ab518e.

[47] Orriere, T. *Confinement Micrométrique Des Décharges Pulsées Nanosecondes Dans l'air à Pression Atmosphérique et Effets Électro-Aérodynamiques*. https://theses.hal.science/tel-01992584, Université de Poitiers, PhD Thesis, in French, 2018.

[48] Macheret, S. O., Shneider, M. N., and Miles, R. B. "Modeling of Air Plasma Generation by Repetitive High-Voltage Nanosecond Pulses." *IEEE Transactions on Plasma Science*, Vol. 30, No. 3, 2002, pp. 1301–1314. https://doi.org/10.1109/TPS.2002.802142.

[49] Popov, N. A. "Kinetics of Plasma-Assisted Combustion: Effect of Non-Equilibrium Excitation on the Ignition and Oxidation of Combustible Mixtures." *Plasma Sources Science and Technology*, Vol. 25, No. 4, 2016, p. 043002. https://doi.org/10.1088/0963-0252/25/4/043002.

[50] Bak, M. S., and Cappelli, M. A. "A Reduced Set of Air Plasma Reactions for Nanosecond Pulsed Plasmas." *IEEE Transactions on Plasma Science*, Vol. 43, No. 4, 2015, pp. 995–1001. https://doi.org/10.1109/TPS.2015.2409300.

[51] Flitti, A., and Pancheshnyi, S. "Gas Heating in Fast Pulsed Discharges in N 2 –O 2 Mixtures." *The European Physical Journal Applied Physics*, Vol. 45, No. 2, 2009, p. 21001. https://doi.org/10.1051/epjap/2009011.

[52] Aleksandrov, N. L., Kindysheva, S. V, Nudnova, M. M., and Starikovskiy, A. Y. “Mechanism of Ultra-Fast Heating in a Non-Equilibrium Weakly Ionized Air Discharge Plasma in High Electric Fields.” *Journal of Physics D: Applied Physics*, Vol. 43, No. 25, 2010, p. 255201. https://doi.org/10.1088/0022-3727/43/25/255201.

[53] Kossyi, I. A., Kostinsky, A. Y., Matveyev, A. A., and Silakov, V. P. “Kinetic Scheme of the Non-Equilibrium Discharge in Nitrogen-Oxygen Mixtures.” *Plasma Sources Science and Technology*, Vol. 1, No. 3, 1992, pp. 207–220. https://doi.org/10.1088/0963-0252/1/3/011.

[54] Capitelli, M., Ferreira, C. M., Gordiets, B. F., and Osipov, A. I. *Plasma Kinetics in Atmospheric Gases*. Springer Berlin Heidelberg, Berlin, Heidelberg, 2000.

[55] Dumitrache, C., Gallant, A., Minesi, N., Stepanyan, S., Stancu, G. D., and Laux, C. O. “Hydrodynamic Regimes Induced by Nanosecond Pulsed Discharges in Air: Mechanism of Vorticity Generation.” *Journal of Physics D: Applied Physics*, Vol. 52, No. 36, 2019, p. 364001. https://doi.org/10.1088/1361-6463/ab28f9.

[56] Cont-Bernard, D. Del, Ruchkina, M., Ding, P., Bood, J., Ehn, A., and Lacoste, D. A. “Femtosecond Two-Photon Laser-Induced Fluorescence Imaging of Atomic Hydrogen in a Laminar Methane–Air Flame Assisted by Nanosecond Repetitively Pulsed Discharges.” *Plasma Sources Science and Technology*, Vol. 29, No. 6, 2020, p. 065011. https://doi.org/10.1088/1361-6595/ab9234.

[57] Griem, H. R. *Plasma Spectroscopy*. McGraw-Hill Book Company, New York, 1964.

[58] Laux, C. O., Spence, T. G., Kruger, C. H., and Zare, R. N. “Optical Diagnostics of Atmospheric Pressure Air Plasmas.” *Plasma Sources Science and Technology*, Vol. 12, 2003, pp. 125–138. https://doi.org/10.1088/0963-0252/12/2/301.

[59] Gigosos, M. A., González, M. Á., and Cardeñoso, V. “Computer Simulated Balmer-Alpha, -Beta and -Gamma Stark Line Profiles for Non-Equilibrium Plasmas Diagnostics.” *Spectrochimica Acta - Part B Atomic Spectroscopy*, Vol. 58, No. 8, 2003, pp. 1489–1504. https://doi.org/10.1016/S0584-8547(03)00097-1.

[60] Konjević, N., Ivković, M., and Sakan, N. “Hydrogen Balmer Lines for Low Electron Number Density Plasma Diagnostics.” *Spectrochimica Acta Part B: Atomic Spectroscopy*, Vol. 76, 2012, pp. 16–26. https://doi.org/10.1016/J.SAB.2012.06.026.

[61] Bastien, F., and Marode, E. “Stark Broadening of Hα and Hβ in Ionized Gases with Space-Charge Field.” *Journal of Quantitative Spectroscopy and Radiative Transfer*, Vol. 17, No. 4, 1977, pp. 453–469. https://doi.org/10.1016/0022-4073(77)90093-0.

[62] Parkevich, E. V, and Khirianova, A. I. “On the Possible Threshold Character of the Spark Microstructure Formation.” *Bulletin of the Lebedev Physics Institute*, Vol. 49, No. 9, 2022, pp. 302–306. https://doi.org/10.3103/S1068335622090068.

[63] Sher, E., Ben-Ya’ish, J., and Kravchik, T. “On the Birth of Spark Channels.” *Combustion and flame*, Vol. 89, No. 2, 1992, pp. 186–194. https://doi.org/10.1016/S0304-419X(01)00029-4.

[64] Modest, M. F. (Michael F. ., and Mazumder, S. *Radiative Heat Transfer*. Academic Press, 2021.

[65] Specair. Specair 3.0. *http://www.spectralfit.com*. http://www.spectralfit.com.

[66] Levko, D., and Raja, L. L. “Early Stage Time Evolution of a Dense Nanosecond Microdischarge Used in Fast Optical Switching Applications.” *Physics of Plasmas*, Vol. 22, No. 12, 2015, p. 123518. https://doi.org/10.1063/1.4939022.

[67] Levko, D., and Raja, L. L. “High-Voltage Microdischarge as a Source of Extreme Density Plasma.” *Physics of Plasmas*, Vol. 25, No. 1, 2018, p. 13509. https://doi.org/10.1063/1.5017594.

[68] Levko, D., Krasik, Y. E., and Tarasenko, V. F. “Present Status of Runaway Electron Generation in Pressurized Gases During Nanosecond Discharges.” *International Review of Physics (I.R.E.PHY.)*, Vol. 6, No. March, 2012, pp. 165–195.

[69] De Giacomo, A., Gaudiuso, R., Dell'Aglio, M., and Santagata, A. "The Role of Continuum Radiation in Laser Induced Plasma Spectroscopy." *Spectrochimica Acta - Part B Atomic Spectroscopy*, Vol. 65, No. 5, 2010, pp. 385–394. https://doi.org/10.1016/j.sab.2010.03.016.

[70] Minesi, N., Stepanyan, S. A., Mariotto, P. B., Stancu, G.-D., and Laux, C. O. On the Arc Transition Mechanism in Nanosecond Air Discharges. No. 2019, 2019, pp. 0463.

[71] Yong, T., Abdalla, A. I., and Cappelli, M. A. "Laser Absorption Measurements of Electron Density in Nanosecond-Scale Atmospheric Pressure Pulsed Plasmas." *Physics of Plasmas*, Vol. 28, No. 5, 2021, p. 053501. https://doi.org/10.1063/5.0035067.

[72] Bastiaans, G. J., and Mangold, R. A. "The Calculation of Electron Density and Temperature in Ar Spectroscopic Plasmas from Continuum and Line Spectra." *Spectrochimica Acta Part B: Atomic Spectroscopy*, Vol. 40, No. 7, 1985, pp. 885–892. https://doi.org/10.1016/0584-8547(85)80059-8.

[73] Iordanova, E., Palomares, J. M., Gamero, A., Sola, A., and van der Mullen, J. J. A. M. "A Novel Method to Determine the Electron Temperature and Density from the Absolute Intensity of Line and Continuum Emission: Application to Atmospheric Microwave Induced Ar Plasmas." *Journal of Physics D: Applied Physics*, Vol. 42, No. 15, 2009, p. 155208. https://doi.org/10.1088/0022-3727/42/15/155208.

[74] Wilbers, A. T. M., Kroesen, G. M. W., Timmermans, C. J., and Schram, D. C. "The Continuum Emission of an Arc Plasma." *Journal of Quantitative Spectroscopy and Radiative Transfer*, Vol. 45, No. 1, 1991, pp. 1–10. https://doi.org/10.1016/0022-4073(91)90076-3.

[75] Sutherland, R. S. "Accurate Free-Free Gaunt Factors for Astrophysical Plasmas." *Monthly Notices of the Royal Astronomical Society*, Vol. 300, No. 2, 1998, pp. 321–330. https://doi.org/10.1046/j.1365-8711.1998.01687.x.

[76] Karzas, W. J., and Latter, R. "Electron Radiative Transitions in a Coulomb Field." *The Astrophysical Journal Supplement Series*, Vol. 6, 1961, p. 167. https://doi.org/10.1086/190063.

[77] Minesi, N. *Thermal Spark Formation and Plasma-Assisted Combustion by Nanosecond Repetitive Discharges*. Université Paris-Saclay, PhD Thesis, 2020.

[78] Pancheshnyi, S. V, Eismann, B., Hagelaar, G. J. M., and Pitchford, L. C. Computer Code ZDPlasKin. http://www.zdplaskin.laplace.univ-tlse.fr.

[79] Hagelaar, G. J. M., and Pitchford, L. C. "Solving the Boltzmann Equation to Obtain Electron Transport Coefficients and Rate Coefficients for Fluid Models." *Plasma Sources Science and Technology*, Vol. 14, No. 4, 2005, pp. 722–733. https://doi.org/10.1088/0963-0252/14/4/011.

[80] Hagelaar, G. J. M. "Coulomb Collisions in the Boltzmann Equation for Electrons in Low-Temperature Gas Discharge Plasmas." *Plasma Sources Science and Technology*, Vol. 25, No. 1, 2016, p. 015015. https://doi.org/10.1088/0963-0252/25/1/015015.

[81] www.lxcat.net, retrieved on April 4, 2019. BSR Database. .

[82] www.lxcat.net, retrieved on March 1, 2019. IST-Lisbon Database. .

[83] Itikawa, Y. "Cross Sections for Electron Collisions with Nitrogen Molecules." *Journal of Physical and Chemical Reference Data*, Vol. 35, No. 1, 2006, pp. 31–53. https://doi.org/10.1063/1.1937426.

[84] Anzai, K., Kato, H., Hoshino, M., Tanaka, H., Itikawa, Y., Campbell, L., Brunger, M. J., Buckman, S. J., Cho, H., Blanco, F., Garcia, G., Limão-Vieira, P., and Ingólfsson, O. "Cross Section Data Sets for Electron Collisions with H2, O2, CO, CO2, N2O and H2O." *The European Physical Journal D*, Vol. 66, No. 2, 2012, p. 36. https://doi.org/10.1140/epjd/e2011-20630-1.

[85] Carbone, E., Graef, W., Hagelaar, G., Boer, D., Hopkins, M. M., Stephens, J. C., Yee, B. T., Pancheshnyi, S., van Dijk, J., and Pitchford, L. "Data Needs for Modeling Low-Temperature Non-Equilibrium Plasmas: The LXCat Project, History, Perspectives and a Tutorial." *Atoms*, Vol. 9, No. 1, 2021, p. 16. https://doi.org/10.3390/atoms9010016.

[86] Minesi, N., Mariotto, P., Stancu, G. D., and Laux, C. O. "Role of the Excited Electronic States in the Ionization of Ambient Air by a Nanosecond Discharge." *AIAA Scitech 2020 Forum*, 2020, p. AIAA paper 2020-0437. https://doi.org/10.2514/6.2020-0437.

[87] Bacri, J., and Medani, A. "Electron Diatomic Molecule Weighted Total Cross Section Calculation. III. Main Inelastic Processes for N2 and N2+." *Physica B+C*, Vol. 112, No. 1, 1982, pp. 101–118. https://doi.org/10.1016/0378-4363(82)90136-X.

[88] Wang, Y., Zatsarinny, O., and Bartschat, K. "B-Spline R-Matrix-with-Pseudostates Calculations for Electron-Impact Excitation and Ionization of Nitrogen." *Physical Review A*, Vol. 89, No. 6, 2014, p. 062714. https://doi.org/10.1103/PhysRevA.89.062714.

[89] Tayal, S. S., and Zatsarinny, O. "B -Spline R -Matrix-with-Pseudostates Approach for Excitation and Ionization of Atomic Oxygen by Electron Collisions." *Physical Review A*, Vol. 94, No. 4, 2016, pp. 1–15. https://doi.org/10.1103/PhysRevA.94.042707.

[90] Ciccarino, C. J., and Savin, D. W. "Electron-Impact Ionization of Atomic Nitrogen." *Journal of Thermophysics and Heat Transfer*, Vol. 33, No. 1, 2019, pp. 154–162. https://doi.org/10.2514/1.T5463.

[91] Alberty, R. A., and Silbey, R. J. *Physical Chemistry 1st Edition*. John Wiley & Sons, Inc., 1992.

[92] Dresvin, S. V. *Physics and Technology of Low-Temperature Plasmas*. Iowa City, The Iowa State University, 1977.

[93] Park, C. "Review of Chemical-Kinetic Problems of Future NASA Missions, I: Earth Entries." *Journal of Thermophysics and Heat Transfer*, Vol. 7, No. 3, 1993, pp. 385–398. https://doi.org/10.2514/3.431.

[94] Phelps, A. V. "Report 28 JILA Information Center." *University of Colorado, Boulder*, 1985.

[95] Itikawa, Y. "Cross Sections for Electron Collisions with Oxygen Molecules." *Journal of Physical and Chemical Reference Data*, Vol. 38, No. 1, 2009, pp. 1–20. https://doi.org/10.1063/1.3025886.

[96] Itikawa, Y. "Cross Sections for Electron Collisions with Nitric Oxide." *Journal of Physical and Chemical Reference Data*, Vol. 45, No. 3, 2016, p. 1464. https://doi.org/10.1063/1.4961372.

[97] Yu, L., Pierrot, L., Laux, C. O., and Kruger, C. H. "Effects of Vibrational Nonequilibrium on the Chemistry of Two-Temperature Nitrogen Plasmas." *Plasma Chemistry and Plasma Processing*, Vol. 21, No. 4, 2001, pp. 483–503. https://doi.org/10.1023/A:1012073800284.

[98] Peterson, J. R., Le Padellec, A., Danared, H., Dunn, G. H., Larsson, M., Larson, A., Peverall, R., Strömholm, C., Rosén, S., Af Ugglas, M., and Van Der Zande, W. J. "Dissociative Recombination and Excitation of N+2: Cross Sections and Product Branching Ratios." *Journal of Chemical Physics*, Vol. 108, No. 5, 1998, pp. 1978–1988. https://doi.org/10.1063/1.475577.

[99] Pitchford, L. C., and Phelps, A. V. "Comparative Calculations of Electron-Swarm Properties in N2 at Moderate En Values." *Physical Review A*, Vol. 25, No. 1, 1982, pp. 540–554. https://doi.org/10.1103/PhysRevA.25.540.

[100] Isola, L. M., Gómez, B. J., and Guerra, V. "Determination of the Electron Temperature and Density in the Negative Glow of a Nitrogen Pulsed Discharge Using Optical Emission Spectroscopy." *Journal of Physics D: Applied Physics*, Vol. 43, No. 1, 2010, p. 015202. https://doi.org/10.1088/0022-3727/43/1/015202.

[101] Cosby, P. C. "Electron-Impact Dissociation of Nitrogen." *The Journal of Chemical Physics*, Vol. 98, No. 12, 1993, pp. 9544–9559. https://doi.org/10.1063/1.464385.

[102] Cartwright, D. C., Chutjian, A., Trajmar, S., and Williams, W. "Electron Impact Excitation of the Electronic States of N2. I. Differential Cross Sections at Incident Energies from 10 to 50 EV." *Physical Review A*, Vol. 16, No. 3, 1977, pp. 1013–1040. https://doi.org/10.1103/PhysRevA.16.1013.

[103] Trajmar, S., Register, D. F., and Chutjian, A. "Electron Scattering by Molecules II. Experimental Methods and Data." *Physics Reports*, Vol. 97, No. 5, 1983, pp. 219–356. https://doi.org/10.1016/0370-1573(83)90071-6.

[104] Phelps, A. V, and Pitchford, L. C. "Anisotropic Scattering of Electrons by N2 and Its Effect on Electron

Transport." *Physical Review A*, Vol. 31, No. 5, 1985, pp. 2932–2949. https://doi.org/10.1103/PhysRevA.31.2932.

[105] Kramida, A., Reader, J., Ralchenko, Y., and NIST ASD Team. NIST ASD. *NIST Atomic Spectra Database (ver. 5.6.1)*. https://physics.nist.gov/asd.

[106] Huber, K. P., and Herzberg, G. *Molecular Spectra and Molecular Structure*. Springer US, 1979.

[107] Thomas, J. M., and Kaufman, F. "An Upper Limit on the Formation of NO(X2Pi) in the Reactions N2(A3Sig) + O(3P) and N2(A) + O2(X3SIg) at 298 K." *Journal of Physical Chemistry*, Vol. 100, No. 21, 1996, pp. 8901–8906. https://doi.org/10.1021/jp960164v.

[108] Shkurenkov, I., Burnette, D., Lempert, W. R., and Adamovich, I. V. "Kinetics of Excited States and Radicals in a Nanosecond Pulse Discharge and Afterglow in Nitrogen and Air." *Plasma Sources Science and Technology*, Vol. 23, No. 6, 2014, p. 065003. https://doi.org/10.1088/0963-0252/23/6/065003.

[109] Piper, L. G. "Quenching Rate Coefficients for N2(A′ 1Σ U-)." *The Journal of Chemical Physics*, Vol. 87, No. 3, 1987, pp. 1625–1629. https://doi.org/10.1063/1.453223.

[110] Lo, A., Cessou, A., and Vervisch, P. "Space and Time Analysis of the Nanosecond Scale Discharges in Atmospheric Pressure Air: II. Energy Transfers during the Post-Discharge." *Journal of Physics D: Applied Physics*, Vol. 47, No. 11, 2014, p. 115202. https://doi.org/10.1088/0022-3727/47/11/115202.

[111] Popov, N. A. "Investigation of the Mechanism for Rapid Heating of Nitrogen and Air in Gas Discharges." *Plasma Physics Reports*, Vol. 27, No. 10, 2001, pp. 886–896. https://doi.org/10.1134/1.1409722.

[112] Burnette, D., Montello, A., Adamovich, I. V., and Lempert, W. R. "Nitric Oxide Kinetics in the Afterglow of a Diffuse Plasma Filament." *Plasma Sources Science and Technology*, Vol. 23, No. 4, 2014, p. 045007. https://doi.org/10.1088/0963-0252/23/4/045007.

[113] Balamuta, J., and Golde, M. F. "Formation of Electronically Excited Oxygen Atoms in the Reactions of Ar(3P0,2) and Xe(3P2) Atoms with O2." *Journal of Physical Chemistry*, Vol. 86, No. 14, 1982, pp. 2765–2769. https://doi.org/10.1021/j100211a041.

[114] Salmon, A., Popov, N. A., Stancu, G. D., and Laux, C. O. "Quenching Rate of N(2 P) Atoms in a Nitrogen Afterglow at Atmospheric Pressure." *Journal of Physics D: Applied Physics*, Vol. 51, No. 31, 2018, p. 314001. https://doi.org/10.1088/1361-6463/aace71.

[115] Tawara, H., and Kato, T. Total and Partial Ionization Cross Sections of Atoms and Ions by Electron Impact. *Atomic Data and Nuclear Data Tables*. 2. Volume 36, 167–353. https://www.sciencedirect.com/science/article/pii/0092640X87900143. Accessed Mar. 4, 2019.

[116] Shcherbanev, S., Krzymuski, T., Xiong, Y., and Noiray, N. "Jetting Axial FLow Induced by Nanosecond Repetitively Pulsed Discharges in Quiescent Ambient Air." *Journal of Physics D: Applied Physics*, Vol. 167, No. 10, 2022, p. 100532. https://doi.org/10.1088/1361-6463/ac7dcd.

[117] Shneider, M. N. "Turbulent Decay of After-Spark Channels." *Physics of Plasmas*, Vol. 13, No. 7, 2006, pp. 1–11. https://doi.org/10.1063/1.2218492.

[118] Dere, K. P., Landi, E., Mason, H. E., Monsignori Fossi, B. C., and Young, P. R. "CHIANTI - an Atomic Database for Emission Lines." *Astronomy and Astrophysics Supplement Series*, Vol. 125, No. 1, 1997, pp. 149–173. https://doi.org/10.1051/aas:1997368.

[119] Dere, K. P., Zanna, G. Del, Young, P. R., Landi, E., and Sutherland, R. S. "CHIANTI—An Atomic Database for Emission Lines. XV. Version 9, Improvements for the X-Ray Satellite Lines." *The Astrophysical Journal Supplement Series*, Vol. 241, No. 2, 2019, p. 22. https://doi.org/10.3847/1538-4365/ab05cf.

[120] Verner, D. A., Ferland, G. J., Korista, K. T., and Yakovlev, D. G. "Atomic Data for Astrophysics. II. New Analytic FITS for Photoionization Cross Sections of Atoms and Ions." *The Astrophysical Journal*, Vol. 465, 1996, p. 487. https://doi.org/10.1086/177435.

[121] Annaloro, J., Teulet, P., Bultel, A., Cressault, Y., and Gleizes, A. “Non-Uniqueness of the Multi-Temperature Law of Mass Action. Application to 2T Plasma Composition Calculation by Means of a Collisional-Radiative Model.” *The European Physical Journal D*, Vol. 71, No. 12, 2017, p. 342. https://doi.org/10.1140/epjd/e2017-80284-5.